



Utilization of AlphaFold models for drug discovery: Feasibility and challenges. Histone deacetylase 11 as a case study

Fady Baseliou, Dina Robaa, Wolfgang Sippl^{*}

Department of Medicinal Chemistry, Institute of Pharmacy, Martin-Luther-University of Halle-Wittenberg, Halle (Saale), Germany

ARTICLE INFO

Keywords:

AlphaFold model
HDAC11
AlphaFill
Model optimization
Drug design and discovery
Docking
Molecular dynamics simulation

ABSTRACT

Histone deacetylase 11 (HDAC11), an enzyme that cleaves acyl groups from acylated lysine residues, is the sole member of class IV of HDAC family with no reported crystal structure so far. The catalytic domain of HDAC11 shares low sequence identity with other HDAC isoforms which complicates the conventional template-based homology modeling. AlphaFold is a neural network machine learning approach for predicting the 3D structures of proteins with atomic accuracy even in absence of similar structures. However, the structures predicted by AlphaFold are missing small molecules as ligands and cofactors. In our study, we first optimized the HDAC11 AlphaFold model by adding the catalytic zinc ion followed by assessment of the usability of the model by docking of the selective inhibitor FT895. Minimization of the optimized model in presence of transplanted inhibitors, which have been described as HDAC11 inhibitors, was performed. Four complexes were generated and proved to be stable using three replicas of 50 ns MD simulations and were successfully utilized for docking of the selective inhibitors FT895, MIR002 and SIS17. For SIS17, The most reasonable pose was selected based on structural comparison between HDAC6, HDAC8 and the HDAC11 optimized AlphaFold model. The manually optimized HDAC11 model is thus able to explain the binding behavior of known HDAC11 inhibitors and can be used for further structure-based optimization.

1. Introduction

HDAC11 is the smallest member of the histone deacetylase family and it is the sole member of class IV and one of the least studied HDAC isoforms [1]. It is mainly expressed in the skeletal muscle, heart, kidney, and brain tissues [2] with potential preferential expression in the gall bladder [3]. Additionally, HDAC11 can be secreted by pancreatic beta cells [4] and interacts with other members of histone deacetylase family to regulate the expression of a number of cytokines [5].

Evidence has demonstrated that HDAC11 is involved in various physiological and pathological processes. HDAC11 is involved in modulating the immune system [6–8] and is a potential target for the treatment of some diseases including multiple sclerosis and viral infection [9]. Moreover, studies showed that HDAC11 knock-out can protect mice from high-fat diet-induced obesity and metabolic syndrome suggesting HDAC11 as an interesting target for the treatment of obesity-related diseases [10,11].

HDAC11 was found to be involved in the modulation of cancer growth and is overexpressed in many cancers, including hepatocellular

[12–15], prostate [16], pituitary [17] and myeloma [18,19]. Additionally, inhibition of HDAC11 showed beneficial effects in neuroblastoma cells [20] indicating that HDAC11 can be considered as a target for the treatment of cancer.

Robust and preferential defatty-acylase activity for HDAC11 was identified. The defatty-acylase activity is > 10,000 times more efficient than its deacetylase activity, concluding that it may represent the major enzymatic activity in vivo [9,21–23].

Several HDAC11 inhibitors were described in the literature, however demonstrating variation in IC₅₀ values when varying the substrate (acetyl/trifluoroacetyl vs. myristoyl peptides from different proteins) used in the enzymatic assay. For example, Kutil et al. re-evaluated the inhibitory activity of reported HDAC11 inhibitors utilizing a myristoylated peptide (peptide 1), which is structurally closer to the myristoylated in vivo substrates [23]. This substrate was derived from the known myristoylation site TNF α -Lys20 in which the naturally occurring threonine residue is replaced by the quencher L-3-nitrotyrosine and the lysine side chain corresponding to Lys20 of TNF α is acylated with fluorescent N-anthraniloylated 11-aminoundecanoic acid.

^{*} Corresponding author.

E-mail address: wolfgang.sippl@pharmazie.uni-halle.de (W. Sippl).

In this study Trapoxin A showed an IC_{50} in the nanomolar range ($IC_{50} = 10$ nM) vs. an IC_{50} of 170 nM using a myristoylated peptide substrate [22]. Fimepinostat, another reported HDAC11 inhibitor could retain an IC_{50} in the nanomolar range when assayed using peptide 1 ($IC_{50} = 23$ nM) and a trifluoroacetylated substrate ($IC_{50} = 5.4$ nM) [24]. Meanwhile, Quisinostat activity dropped from the nanomolar range to single digit micromolar IC_{50} when using myristoylated peptide 1 ($IC_{50} = 3270$ nM) [23] as a substrate rather than an acetylated peptide ($IC_{50} = 0.37$ nM) [25]. For the pan-HDAC inhibitor TSA, higher drop in activity was observed when using myristoylated peptide 1 ($IC_{50} = 22000$ nM) instead of the acetylated fluorogenic pentapeptide ($IC_{50} = 17.3$ nM) substrate [26], which show agreement with obtained IC_{50} using myristoylated substrate ($IC_{50} = 32000$ nM) [22]. Several inhibitors that were reported in literature were also re-tested for their inhibitory activity of HDAC11 using the substrates considered in the current study and showed different activities [23].

While Trapoxin A, Quisinostat and TSA are non-selective inhibitors of HDAC11, there are few selective inhibitors that were described in literature. FT895 showed same variation as discussed above as it exhibited activity in a low nanomolar range ($IC_{50} = 3$ nM) [27] when assayed using a trifluoroacetyl lysine peptide, while when assayed using the physiological myristoyl lysine substrate, activity of sub-micromolar range was observed ($IC_{50} = 740$ nM) [28]. The alkyl hydrazide inhibitor SIS17 [28] inhibited HDAC11 at a sub-micromolar range ($IC_{50} = 830$ nM). Recently Trapoxin A analogues bearing long alkyl chains were developed as potent and selective HDAC11 inhibitors with the most active compound TD034 showing activity in low nanomolar range using myristoylated H3K9 peptide as substrate ($IC_{50} = 5.1$ nM) [29]. MIR002 [30] showed inhibition of HDAC11 in micromolar range ($IC_{50} = 6090$ nM) using trifluoroacetyl lysine substrate indicating for weak inhibition. Therefore, for modeling studies it is recommended to use and compare only inhibitors and in vitro values that have been tested in the same assay/laboratory.

Computer aided drug design (CADD) combines various molecular modeling techniques that are used to design and discover new molecules bearing bio-molecular activities [31,32]. The combination of molecular docking, molecular dynamics simulations and de novo design approaches have significantly contributed to the conventional drug discovery processes by reducing time and resources required for hit identification and lead optimization phases [33]. Sabe and coauthors in their review [32] listed around 70 approved drugs for which the development process included one or several computational methods including molecular docking, structure-based design, structure-based virtual screening, ligand-based pharmacophore screening, homology modeling, quantitative structure activity relationship studies and molecular dynamics simulations. In most of these discoveries, the initial hit or lead was identified using CADD [32]. One limitation to the structure based drug design is the shortage of structural data for the target protein, a challenge that can be solved with the aid of homology modeling technique [34].

So far no crystal structure of HDAC11 has been reported. The catalytic core region of HDAC11 shares sequence similarity to class I and class II HDAC members, however, comparison over the full length of the protein shows that HDAC11 is only slightly homologous to other HDAC family members [1,2]. Calculating the sequence identity for HDAC11 with the primary sequences of the catalytic domains available in the PDB databank for other human HDAC isoforms, shows low sequence identity percent ranging between 16 % and 22 %. This lowers the probability to get a reliable homology model via template based folding and suggests that applying a different approach for the prediction of the 3D structure of HDAC11 as AlphaFold is of advantage.

AlphaFold is a neural network machine learning approach for predicting the 3D structures of proteins and it was shown to predict protein structures with atomic accuracy even in absence of known similar structures [35].

The database of the 3D structures of the whole human proteome was

constructed by AlphaFold and it includes HDAC11 model. While the AlphaFold predictions in general provide improved accuracy when compared to template based homology modeling [36], the models from AlphaFold should be carefully considered when used for docking or drug design studies because the folding is predicted in absence of ligands and cofactors as zinc ion in the case of HDAC11.

Trying to solve this problem, AlphaFill [37] introduced an algorithm for enrichment of the models in the AlphaFold database by transplanting such small molecules and ions utilizing structure and sequence similarity with experimentally determined protein structures.

In order to assess the usability of the AlphaFold HDAC11 model for the aim of drug discovery, the available AlphaFill results for HDAC11 were analyzed. Since the findings from this analysis were not satisfactory, we considered the optimization of the AlphaFold model of HDAC11 by adding the zinc ion and minimization of model-ligand complexes obtained by merging three selected, previously described potent HDAC11 inhibitors for which X-ray structures with the related HDAC8 are available, namely, Trapoxin A (PDB 5VI6) [38], Quisinostat (PDB 6HSK and 6HSH) [39] and TSA (PDB 5D1B) [40] (Fig. 1). While the selected ligands show variation in the inhibitory activity for HDAC11 as discussed above, scaffold diversity of the selection was meant to expand the chances of obtaining an optimized complex that can further be used for drug discovery. The obtained HDAC11-ligand complexes were further utilized for docking of HDAC11 selective inhibitors, FT895 and MIR002. The obtained HDAC11-ligand complexes as well as the poses obtained from the docking study were subjected to classical molecular dynamics simulation to assess the stability of the optimized model as well as the obtained ligand poses. As the defatty-acylase activity preference of HDAC11 is confirmed, the presence of the so called foot pocket that theoretically accommodates the longer alkyl chain was explored. For this purpose stepwise docking and minimization of the reported selective HDAC11 ligand SIS17 which bears a 16 carbon alkyl chain as well as docking in loop 1 remodeled AlphaFold model were performed.

2. Materials and methods

Schrodinger Suite 2019 was used for all modeling work except zinc ion docking into the homology model. Maestro [41] was utilized for visualization.

The AlphaFold HDAC11 model was obtained from the AlphaFold website (<https://alphafold.ebi.ac.uk/entry/Q96DB2/>).

2.1. Protein preparation

All protein structures were preprocessed using Protein Preparation Wizard [42,43] by adding hydrogens and assigning bond orders. Zero order bonds to metals were created and water beyond 5 Å from the ligands was deleted. Ionization states of the ligands were generated using Epik [44–46] at pH 7.0 ± 2.0 . For crystal structures with hydroxamic acid inhibitors (PDB 6HSK, 6HSH and 5D1B), the hydroxamate form was selected for further hydrogen bond optimization and minimization. Hydrogen bond optimization was assigned automatically with sampling water orientation and using PROPKA at pH 7.0. Restrained minimization was performed with RMSD cutoff of 0.3 Å for heavy atoms using the OPLS3e force field [47–50].

2.2. Ligand preparation

Ligands including the original ligands were prepared utilizing Lig-Prep [51] panel with OPLS3e force fields. Hydroxamic acid ligands were prepared in the deprotonated form, while other ligands were prepared in the neutral form. No further ionization states, tautomers or isomers were generated.

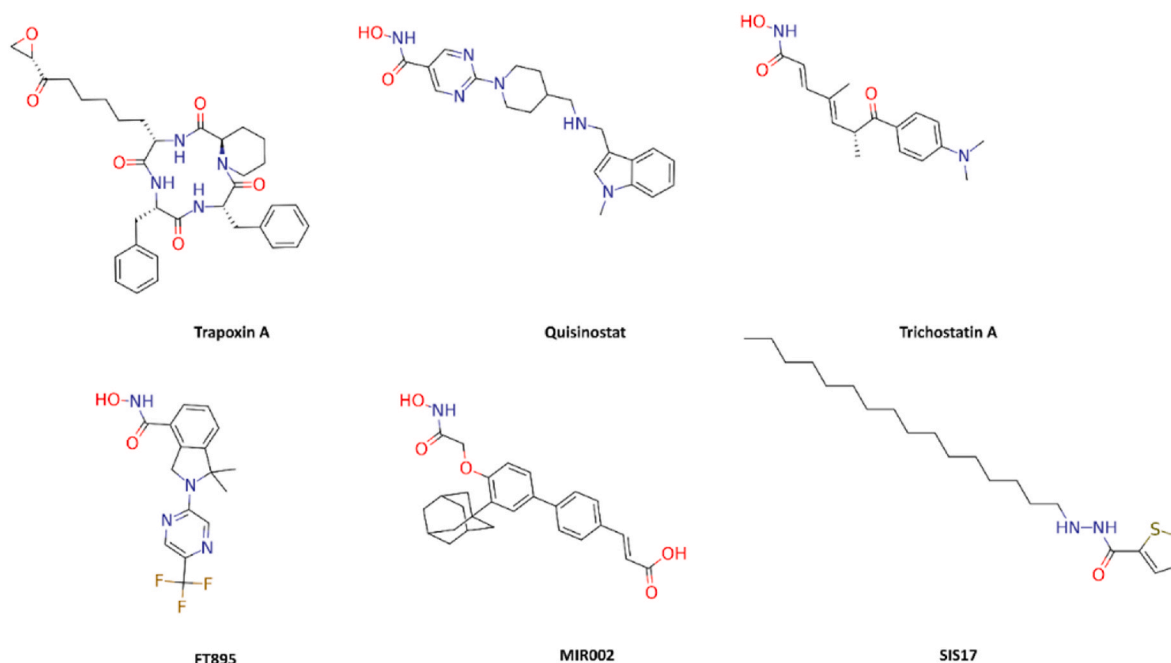


Fig. 1. Structures of HDAC inhibitors included in this study.

2.3. Model optimization

2.3.1. Zinc ion docking

The zinc ion was docked using the Metal Ion-Binding Site Prediction and Docking Server (MIB) (<http://bioinfo.cmu.edu.tw/MIB/>) and the top scored model was selected for further optimization.

2.3.2. Coordination distance optimization

The obtained model was then prepared using the protein preparation settings mentioned above. Protonation states of titratable residues in the catalytic pocket were assigned. To adjust the coordination distance, refinement of loop 4 was performed. Loop 4 (residues: 180–185) was refined using Prime Refine Loops panel [52–54], with extended loop sampling and generating 10 structures. The structure with the lowest potential energy was then selected for further utilization. Preparation and restrained minimization were performed for the selected refined model using the settings stated above.

2.4. Site mapping

Site mapping of the AlphaFold HDAC11 with the zinc ion was performed using SiteMap [55–57] panel and by identifying top ranked potential receptor binding sites. The site mapping was performed for two models with different Phe152 rotamers with reporting up to five sites and requiring at least 15 site points per reported site. The top ranked site map for each model was used to generate grid for docking.

2.5. Binding site optimization

2.5.1. Placing ligands

The prepared and minimized crystal structures were aligned to the refined AlphaFold model using Protein Structure Alignment panel and selecting all residues as reference residues. The ligand from the crystal structure was then placed into the AlphaFold model by merging.

2.5.2. Unrestrained minimization

All model-ligand complexes were solvated in SPC water model using an orthorhombic box and 10 Å distance between the solute structures and the simulation box boundary. The box volume was then minimized.

The system was neutralized by adding chloride ions that were placed 4 Å away from the ligand.

The complexes were then minimized using Minimization panel from Desmond [58,59], each for 100 ps without restraints.

2.6. Remodeling loop 1

Loop 1 (residues 21–40) of the TSA-HDAC11 AlphaFold model was remodeled using HDAC6 (PDB 5EDU) as template and by utilizing the Build Homology Model Panel in the Multiple sequence viewer. A knowledge based model was generated utilizing the composite/chimera option in presence of TSA as ligand. The generated homology model was then preprocessed and restrained minimization was further applied using the same settings as mentioned above to resolve overlapping atoms.

2.7. Grid generation

Receptor grids were generated using the Receptor Grid Generation panel. In case of the apoform receptor, the site map was used to generate the grids. While for the optimized complexes, the centroid of the complexed ligand was used. For the apoform and each of the optimized complexes, two grids were generated utilizing the original and the flipped-out Phe152 rotamers (lowest energy rotamer). For docking of the hydroxamic acid ligands, FT895 and MIR002, grids were generated with the protonated His142 in HIP state, while for SIS17, grids with the HID state were generated. For SIS17, dock ligands with length ≥ 20 Å option was selected.

For the docking of SIS17 in the TSA-HDAC11- AlphaFold model with remodeled loop 1 the inner box (ligand diameter midpoint box) length were set to be 15 Å for each side.

2.8. Docking

2.8.1. Docking of hydroxamic acid inhibitors

All hydroxamic acid inhibitors were docked in the hydroxamate form. Initially, FT895 was docked in the two grids obtained from the site mapping of the apoform and as these results were not satisfactory the docking was further tried with the 8 grids generated from the optimized

complexes. For all trials, docking was performed using Glide [60–63] with standard precision mode and flexible ligand sampling utilizing OPLS3e force field.

For MIR002, docking was performed in the grid obtained from TSA-HDAC11 AlphaFold model complex with flipped-out Phe152 as it showed the best performance regarding the docking of FT895. Different settings were applied for each ligand regarding the output. For FT895 and MIR002, top-ranked docking poses were subjected to post-docking minimization.

2.8.2. Docking of alkyl hydrazide inhibitors

Initial docking of SIS17 was performed in the 8 grids using standard precision mode and flexible ligand sampling utilizing OPLS3e force field and specifying 5 poses to be subjected to post-docking minimization and reporting a single top scored pose.

For the stepwise docking and minimization process, docking of SIS17 was performed using two grids, obtained from TSA-HDAC11 AlphaFold complex, one grid with the original Phe152 rotamer and the other with the flipped-out rotamer. A series of 16 SIS17 derivatives were generated virtually, starting with a single carbon as alkyl chain substitution to the hydrazide moiety and increasing one carbon atom at a time till reaching the original ligand SIS17 with 16 carbon alkyl chain.

For each grid the series was docked with standard precision mode and flexible ligand sampling utilizing OPLS3e force field and specifying 100 poses to be subjected to post-docking minimization and reporting a single top scored pose. For each grid the pose of the ligand with the maximum alkyl chain length (1 carbon alkyl chain ligand for the grid with original Phe152 rotamer and 5 carbon alkyl chain ligand for the flipped lowest energy Phe152 rotamer) that could show a bidentate chelation mode (distance to zinc ion less than 2.6 Å) was selected as core containing molecule to be utilized as reference pose for restricted docking of ligands with longer alkyl chains using maximum common substructure and same output settings as mentioned above.

The ligands poses with maximum alkyl chain length that could fit with a bidentate chelation mode using the core restricted method in complex with the HDAC11 AlphaFold model (13 carbon alkyl chain ligand for the grid with original Phe152 rotamer and 11 carbon alkyl chain ligand for the flipped-out Phe152 rotamer) were then subjected to minimization using Desmond Minimization panel and same settings as reported above.

The obtained poses from the Desmond minimization step were further used for core restricted docking of the ligands that could not fit in the first core restricted docking step. While this was successful to place the SIS17 for the grid with the original Phe152 rotamer, further alignment of SIS17 to the longest alkyl chain virtual derivative that could fit (14 alkyl chain ligand) was performed for the grid with flipped-out Phe152 rotamer using Flexible Ligand Alignment panel. The obtained poses were then subjected again to Desmond minimization.

SIS17 was also docked in the TSA-HDAC11- AlphaFold model with remodeled loop 1 using standard precision mode and flexible ligand sampling utilizing OPLS3e force field and specifying 100 poses to be subjected to post-docking minimization and reporting a single top scored pose.

2.9. Molecular dynamics simulation

The optimized apoform before further optimization of the binding site as well as the four optimized complexes and the selected docking poses were subjected to molecular dynamics simulation using Desmond. Each pose was simulated for 50 ns and the simulation was repeated three times for each pose applying different random seeds. The poses of the selective ligands FT895 and MIR002 as well as the vertical pose of SIS17 were further subjected to 500 ns molecular dynamics simulations. For SIS17 poses, zero order bonds to the metal were created using Protein Preparation Panel before submitting to system preparation. The system was solvated in SPC water model using an orthorhombic box and 10 Å

distance between the solute structures and the simulation box boundary. The box volume was then minimized. The system was neutralized by adding chloride ions that were placed 4 Å away from the ligand.

The prepared system was relaxed using the default Desmond relaxation protocol for NPT ensemble followed by a production run utilizing the NPT ensemble at the temperature of 300 K using a Nose-Hoover chain thermostat and pressure of 1.01325 bar using Martyna-Tobias-Klein barostat. The progress of the simulation was recorded every 100 ps.

For analysis, the Simulation Event Analysis panel was used for RMSD and distance calculations. The RMSD of the protein was calculated using the backbone atoms while the ligand and zinc ion RMSD was calculated by fitting to the protein backbone. The Simulation Interaction Diagram panel was used for analyzing the RMSF and the interaction persistence (also known as occupancy) of the ligands. RMSD and RMSF of the protein were calculated excluding the termini (residues: 1–14 and 321–347).

3. Results and discussion

3.1. AlphaFill results analysis

As a first step, the quality of the automated approach of AlphaFill in transplanting missing ligands and cofactors was assessed. To this end, the AlphaFill results for HDAC11 AlphaFold model containing compounds transplanted from structures with percent identity up to 25 % were analyzed. While for the catalytic zinc ion, the transplant clash score (TCS) is low as would be expected for a single atom ion but the local RMSD score for two transplants is high showing 2.48 and 6.43 indicating for medium to low confidence for these transplants. Visual inspection of the zinc ion that is transplanted into the binding pocket shows that it is not ideally placed into the binding pocket and subsequently the expected metal ion-coordination by the neighboring residues (Asp181, Asp261 and His183) is partially missing. Distances of 1.42 Å, 3.45 Å and 2.95 Å between the zinc ion and Asp181-OD1, Asp261-OD1 and His183-ND1, respectively, were observed.

Additionally, AlphaFill transplanted four ligands, namely the nonselective inhibitors SAHA, Quisinostat, MS-344 and Trichostatin A (TSA), into the AlphaFold model. All transplants showed medium to low confidence with either local RMSD or the TCS values except for TSA which was transplanted from the HDAC6 crystal structure (PDB ID: 5EDU) [64] and MS-344 which was obtained from the HDAC8 crystal structure (PDB ID 1T67) [65]. While it can be easily understandable why such ligands with alkyl linkers are showing low TCS, the visual inspection (Fig. 2) of the transplanted ligands in the model shows that both are suffering from severe clashes with neighboring residues (His142, Leu268 and Tyr304 for MS-344 and His142, Glu94, Leu268 and Tyr304 for TSA). Furthermore, the zinc ion coordination by the hydroxamic acid moiety of both ligands is not optimal as would be expected due to the misplacement of the zinc ion.

3.2. AlphaFold model optimization

3.2.1. Zinc ion docking and coordination optimization

Since the automated approach using AlphaFill results for HDAC11 were not satisfactory, we adapted another approach for the optimization of the original AlphaFold model. As a first step, the catalytic zinc ion was docked into the AlphaFold model using the MIB server. The top scored model showed that the zinc ion was properly placed at the depth of the lysine-binding pocket and the expected metal coordination pattern by neighboring residues could be observed. The distances between the zinc ion and the coordinating residues were 2.04 Å, 1.55 Å and 2.00 Å for Asp181-OD1, His183-ND1 and Asp261-OD1, respectively (Fig. 3). While the distance between the zinc ion and both Asp181 and Asp261 is within the range observed in crystal structures of other histone deacetylase isoforms from class I and II, the distance to His183 of 1.55 Å is lower

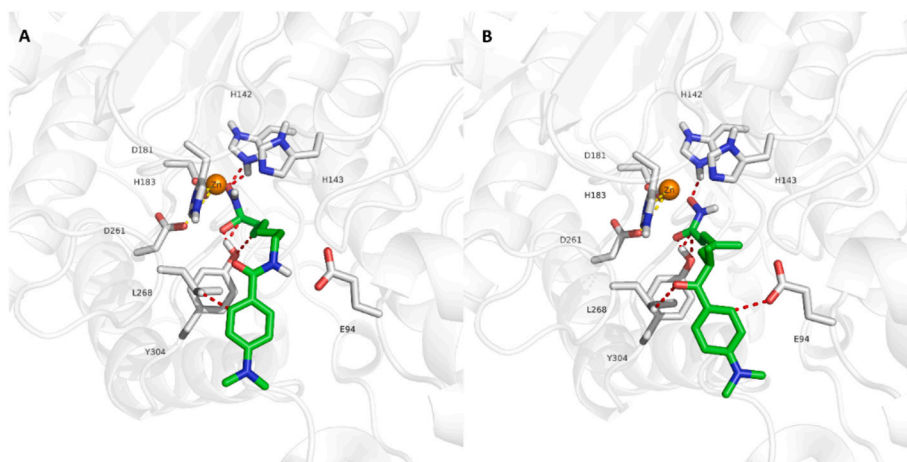


Fig. 2. AlphaFill transplants showing non-optimal zinc ion coordination and clashes between the ligands and the protein. The protein backbone is represented as white cartoon, the zinc ion as orange sphere, the binding site residues as grey sticks and the ligands as green sticks. Coordination bonds are represented as yellow dashed lines and clashes as red dashed lines. **A** and **B** are MS-344 and TSA respectively.

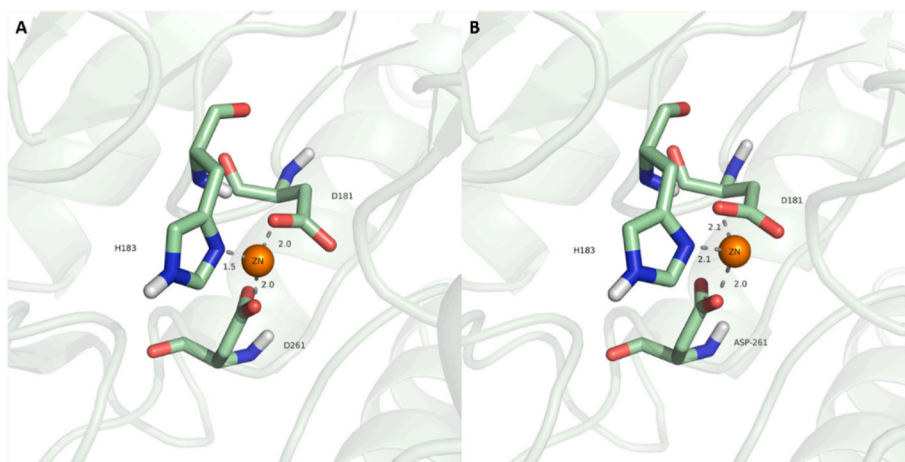


Fig. 3. Zinc ion coordination optimization. **A**, the top scored model from zinc ion docking using MIB server showing shorter distance to His183 than that observed in crystal structures from other HDAC family members. **B**, the optimized model showing coordination distances in agreement with the experimentally observed distances.

than the expected value. By refinement of loop 4 (residues: 180–185) (**Methods section 3.2**), a model with reasonably coordinated zinc ion (2.05 Å, 2.07 Å and 2.03 Å for Asp181, His183 and Asp261, respectively) was obtained.

Three runs of molecular dynamics simulation each of 50 ns were performed in order to assess the stability of the protein and the docked zinc ion which was confirmed as the RMSD for both the protein and zinc ion is stabilizing below 2 Å (**Fig. S1**).

RMSF plot of the three runs shows the fluctuations of the surface-exposed loops with RMSF for loop 1 and 2 reaching up to 2 Å whereas for loops 5 and 6, RMSF between 2 Å and 2.5 Å was observed. While such values can be expected for long loops that are solvent-exposed, other regions of the protein show RMSF-values almost below 1 Å confirming the protein stability (**Fig. S2**).

Docking of the selective HDAC11 inhibitor FT895 into the optimized AlphaFold model containing the zinc ion, however, failed and no poses could be generated, a result that goes in agreement with previous studies evaluating the usability of AlphaFold models for docking. In one study, docking of the original ligands was used to compare the performance of 2474 AlphaFold predictions and their corresponding crystal structures. Re-docking in crystal structures showed success rate of 41 % compared to 17 % for AlphaFold predictions taking 2 Å as threshold for RMSD

considering the top ranked poses [66]. In another study four docking software were used to assess the accuracy and usefulness of AlphaFold models for docking and drug discovery utilizing a set of 22 targets from diverse protein families. While results demonstrated a worse performance for AlphaFold models when compared to crystal structures, the authors suggested this could be due to large variation in the binding site backbone leading to its distortion or small variations at the backbone or even the side chain levels within the binding site [67]. In agreement with this, it was demonstrated that manipulation of the binding site in terms of inducing flexibility or manual modification of the low confidence regions could enhance the docking results [66].

Analyzing the results of the MD simulation revealed that the side chain of Phe152 shows high fluctuation and can adopt two conformations (**Fig. S3**); a flipped-in and flipped-out conformation. It's worth noting that the flipping of this conserved Phe residue in the lysine binding pocket was also observed in HDAC8 crystal structures (6ODC, 6ODB and 6ODA). Hence, in subsequent docking studies we considered both rotameric forms of Phe152. Docking of FT895 in the generated grid with the Phe152 rotamer flipped-out of the pocket, resulted in a pose that could not reach the zinc ion in the depth of the binding site and none of the expected interactions were observed (**Fig. 4**). It hence appeared that the binding site in the AlphaFold model needs further optimization

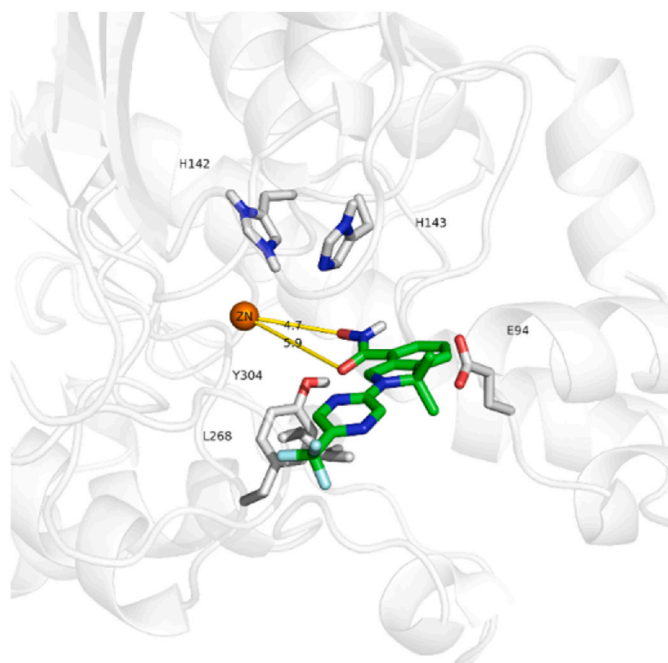


Fig. 4. Docked pose of FT895 in the model with the optimized coordination of the zinc ion and flipped-out Phe152 without further binding site optimization. The inhibitor is not able to coordinate to the zinc ion. The protein backbone is represented as white cartoon, the interacting binding site residues as grey sticks, zinc ion as orange sphere and the ligands as green sticks.

in presence of active ligands prior docking studies.

3.2.2. Binding site optimization

Since docking of the selective HDAC11 inhibitor FT895 in the optimized AlphaFold model was not successful, further optimization of the binding site was considered mandatory. To this end, we transplanted (Methods section 5.1) three nonselective inhibitors, namely Trapoxin A, Quisinostat and TSA from HDAC8 crystal structures co-crystallized with the respective inhibitor into the model. Subsequently, the protein structure was optimized by minimization of the model in the presence of these different ligands using Desmond minimization.

It's worth noting, that the initial protein-ligand complexes obtained by transplanting Trapoxin A, TSA and Quisinostat into the zinc containing AlphaFold model suffered from severe clashes with the side

chains of some residues lining the binding site, especially Glu94, Phe152, His183, Leu268, and Tyr304. These complexes also suffered from non-optimal chelation of the zinc ion that the hydroxamate moiety of the ligands showed a monodentate chelation of the zinc ion only through the oxygen of the hydroxyl group while for all ligands only a single hydrogen bond was observed to either His142 or His143.

Minimization of these protein-ligand complexes in Desmond (Methods section 5.2) resulted in the removal of the clashes with neighboring residues and optimization of the interactions of the Zn-binding moiety (Figs. 5 and 6). The expected bidentate chelation mode to the catalytic zinc ion was observed for the four HDAC11 AlphaFold protein-ligand complexes with distances between the zinc ion and the chelator ligand atoms ranging between 2.03 Å and 2.16 Å. The hydrogen bonding pattern for the complexed ligands resembles what is commonly observed in HDAC crystal structures. The hydroxamate moiety is showing the three main interactions namely a salt bridge to His142 and hydrogen bond interactions to His143 and Tyr304. For Trapoxin A, the gemdiol zinc binding group forms two hydrogen bond interactions with the side chains of His142 or His143 and Tyr304.

Additional salt bridge and hydrogen bond interactions between each of the protonated-NH group in the linker of Quisinostat from the first pose (transplanted from 6HSH) and the three amide-NH groups in the macrocycle capping group of Trapoxin A, respectively, and the Glu94 side chain were observed. These interactions are missing for TSA, while in the second pose of Quisinostat (transplanted from 6HSK), the methyl indole capping group is aligned towards loop 5 leading to a higher distance allowing only for ionic interactions, compared to the first pose in which the capping group is directed towards loop 2. Pi-Pi interactions are observed in the second pose of Quisinostat between the indole and pyrimidine rings and Tyr209 and Phe152 respectively.

3.3. Docking

3.3.1. Docking of hydroxamic acid inhibitors

3.3.1.1. FT895. In order to examine the usability of the optimized models, docking of the selective ligand FT895 was performed in all eight grids. For the docking, 2 grids for each complex obtained from the previous step were generated with different Phe152 rotamers.

Docking of FT895 was considered successful in three grids as the ligand was placed in the binding site and showing the expected interactions. The best pose in terms of bidentate chelation, hydrogen bond interactions and docking score (Table 1), was obtained by docking in TSA-HDAC11 grid with the flipped-out Phe152 rotamer (Fig. 7A). The

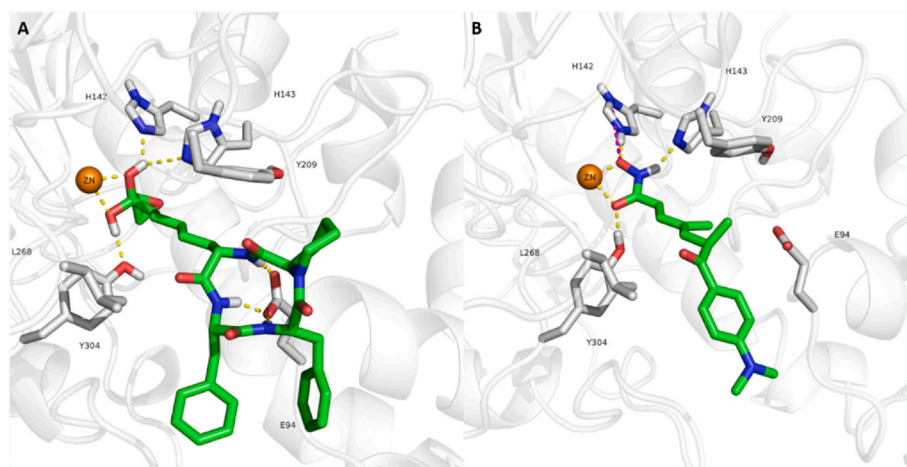


Fig. 5. Desmond minimized poses of ligands used to optimize the HDAC11 AlphaFold model. **A**, Trapoxin A, **B**, TSA. The protein backbone is represented as white cartoon, the interacting binding site residues as grey sticks, zinc ion as orange sphere and the ligands as green sticks. Hydrogen bonds and coordination bonds are represented as yellow dashed lines and the ionic interactions as magenta dashed lines.

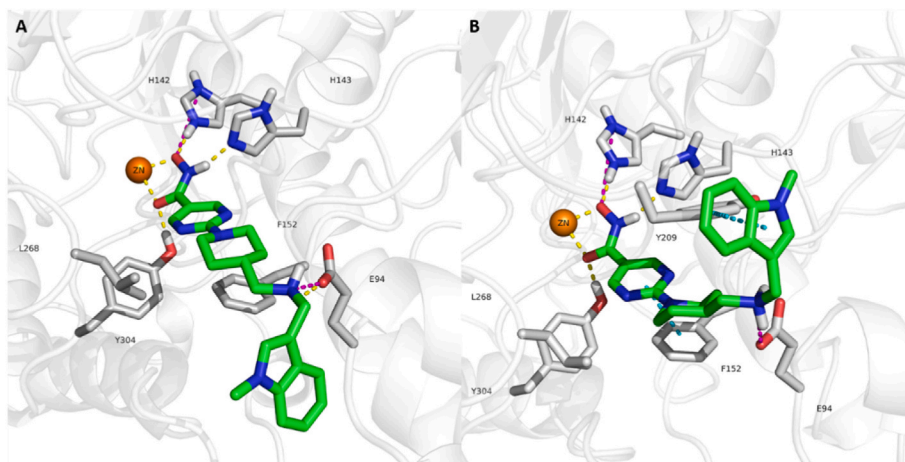


Fig. 6. Desmond minimized poses of ligands used to optimize the HDAC11 AlphaFold model. **A** and **B**, are the first and the second poses of Quisinostat, respectively. The protein backbone is represented as white cartoon, the interacting binding site residues as grey sticks, zinc ion as orange sphere and the ligands as green sticks. Hydrogen bonds and coordination bonds are represented as yellow dashed lines, the ionic interactions as magenta dashed lines and the pi-pi interactions as cyan dashed lines.

Table 1

Docking results of FT895 into the 8 grids generated using the optimized complexes.

Grid	docking score	glide score	glide emodel	Distance to Zn		HB/salt bridge			
				C=O	NO ⁻	His142	His143	Tyr304	
Q1	-5.389	-5.389	-48.833	4.14	2.08		+	+	
Q1-flipped	-4.906	-4.906	-55.088	3.83	2.15				
Q2	-5.325	-5.325	-55.041	4.08	2.11		+	+	
Q2-flipped	-6.967	-6.967	-63.957	2.54	2.16	+	+	+	
Trapoxin	-4.171	-4.171	-44.526	Wrong orientation-Hydroxamic acid facing the solvent					
Trapoxin-flipped	-5.161	-5.161	-52.861	4.17	2.06			+	
TSA	-6.989	-6.989	-70.085	2.97	2.03	+	+	+	
TSA-flipped	-7.979	-7.979	-80.866	2.47	2.16	+	+	+	

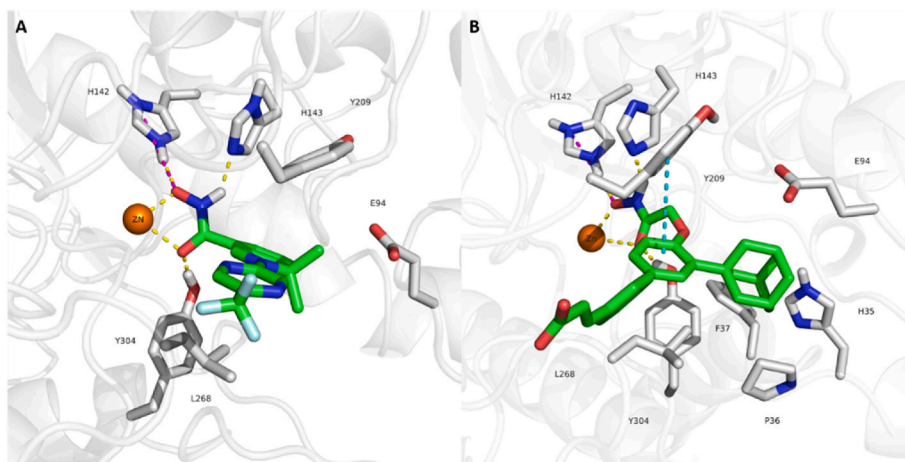


Fig. 7. Docked poses of ligands in the HDAC11 AlphaFold model after binding site optimization. **A** and **B** are FT895 and MIR002, respectively. The protein backbone is represented as white cartoon, the interacting binding site residues as grey sticks, zinc ion as orange sphere and the ligands as green sticks. Hydrogen bonds and coordination bonds are represented as yellow dashed lines, the ionic interactions as magenta dashed lines and the pi-pi interactions as cyan dashed lines.

ligand is showing bidentate chelation of the zinc ion with distances of 2.47 Å and 2.16 Å to the carbonyl and hydroxyl oxygens, respectively. The common salt bridge as well as the two hydrogen bond interactions between the zinc binding group of FT895 and His142, His143 and Tyr304, respectively, were also observed. The linear structure of the ligand is sandwiched between the side chains of Leu268 and Tyr209 with which it forms hydrophobic interactions.

3.3.1.2. MIR002. The HDAC11 selective inhibitor MIR002 was also successfully docked in the optimized AlphaFold model using the TSA-HDAC11 grid with the flipped-out Phe152 rotamer. The obtained pose shows monodentate chelation of the zinc ion with distances of 2.84 Å and 2.07 Å between the zinc ion and the carbonyl and hydroxyl oxygens, respectively. The zinc binding group of the ligand could fulfill the salt bridge and the two hydrogen bond interactions to His142, His143 and Tyr304, respectively (Fig. 7B). In the obtained pose the linear biphenyl

system is accommodated between the side chains of Tyr209 and Leu268 of loop 5 and loop 6, respectively, while the bulky adamantane moiety is directed towards loop 1 and forming hydrophobic interactions with Pro36. Other hydrophobic interactions can also be observed between the biphenyl ring system and Tyr304 and Leu268. Pi-Pi interactions between one of the phenyl rings and Tyr209 can be observed.

3.3.2. Docking of alkyl hydrazide inhibitors

In order to explore the so called foot pocket, docking of the selective ligand SIS17 was performed in all eight generated grids, however the docking was not successful since no reasonable pose could be obtained. In all poses the long 16 carbon alkyl chain was placed out of the pocket and exposed to the solvent (Fig. S4 and S5). For this reason, two different approaches for further optimization of the model were considered, namely, remodeling loop1 and using a stepwise docking and minimization process.

3.3.2.1. Loop 1 remodeling. For the evaluation of the predicted models, AlphaFold uses two methods. The first is per residue confidence score, called predicted local distance difference test (pLDDT), which applies a scale from 0 to 100, and the second score is the predicted aligned error which is useful in assessment of the domain accuracy with expected position error scale in angstrom.

For the HDAC11 model, some residues in loop 1 show low model confidence score ($70 > \text{pLDDT} > 50$) while the whole loop shows expected position error between 25 Å and 30 Å approximately (Fig. 8). While the structural heterogeneity due to loop flexibility can be considered as significant factor, shortage in sequence coverage can also account for such lowered scores [68].

Taking into consideration the AlphaFold scoring, the remodeling of loop 1 of the AlphaFold HDAC11 model was considered. Using HDAC6 as template, a knowledge based hybrid model was generated as described in the Methods section. The model was built in presence of TSA that was previously transplanted into HDAC11 (Fig. 9A).

Docking of SIS17 directly into the grid generated from this model resulted in a pose that is fulfilling the three hydrogen bond interactions with Tyr304, His142 and His143. The bidentate chelation mode was also observed with distances of 2.27 Å and 2.57 Å between the zinc and each of the carbonyl oxygen and the nitrogen of the hydrazide group respectively (Fig. 9B). Interestingly remodeling of loop 1 allowed enough room for the long alkyl chain of SIS17 to be accommodated between loop 1 and loop 7.

3.3.2.2. Docking and refinement by minimization. For the second approach, the final poses of the alkyl hydrazide inhibitor SIS17 obtained

by docking and minimization (Methods section 8.2) of the virtually generated ligand series with varying the alkyl chain length, showed different orientation of the alkyl chain in the two different grids (Fig. 10). The determinant of the direction of the alkyl chain is the rotamer of Phe152. Superposing both poses shows that the stem of the alkyl chain (first five carbons) is accommodated in the same space that is lined with residues Phe37, Gly140, Phe141, His142, His143, Gly151, Phe152, Cys153, Ser301, Gly302 and Tyr304. The branching of the alkyl chain then starts at carbon 6. The original flipped-in Phe152 allows enough space for the alkyl chain to be directed horizontally and accommodated between loop 1 and loop 2. In the second grid, in which the Phe152 is flipped-out of the binding pocket, this direction is blocked and the alkyl chain of SIS17 is directed more deeply into the binding pocket along loop 3 and loop 7.

For both final poses the chelation mode is bidentate through the carbonyl oxygen and the nitrogen of the hydrazide zinc binding group with distances ranging between 2.29 Å and 2.4 Å respectively. The three hydrogen bonds to Tyr304, His142 and His143 are observed in both poses.

While the optimization of the binding site was mandatory for docking in our study. It is worth to note that in recent work by Ren et al. [69], modification to the original CDK20 AlphaFold model was necessary to be useable for the aim of drug discovery, for example the removal of the C terminus that was blocking the solvent exposed region of the protein and occupying the ATP binding pocket through Arg305. However, the reliable identity percentage between CDK20 and related structures from the cyclin dependent kinase family reaching up to around 40 % [70] with multiple crystal structures available in the protein data bank suggests that the template based homology model might have been a more convenient methodology, which is not the case for HDAC11 (Table S1).

3.4. Molecular dynamics simulations

One limitation of the docking approach is ignoring the protein flexibility by treating the protein as rigid body, which limits the ability to guarantee the stability of the observed interactions of a ligand docked pose and rightly predict the binding mode. On the other hand, molecular dynamics (MD) simulation techniques can account for the flexibility of the protein along with solvent effects thus allowing for deeper insight and investigation of the behavior of the ligand and its stability in a dynamic environment. Such information, provides chances for structure based design of better performing ligands. Common objective measures for the analysis of the MD simulation results are root mean square deviation (RMSD), root mean square fluctuation (RMSF) and interactions persistence/occupancy. These measures are used to evaluate protein-

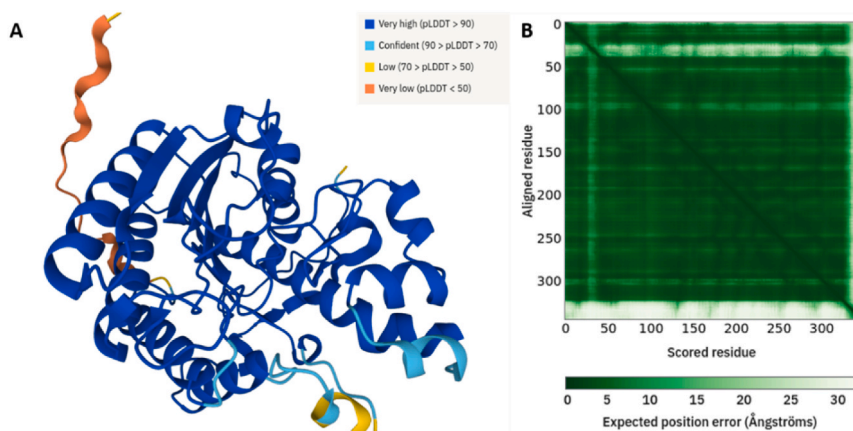


Fig. 8. HDAC11 AlphaFold model scoring. **A**, model cartoon colored according to the per residue confidence score, showing residues of lower scores in loop 1 ($70 > \text{pLDDT} > 50$). **B**, expected position error score showing distance of approximately 25 Å to 30 Å for loop 1. Pictures acquired from AlphaFold website (<https://alphafold.ebi.ac.uk/entry/Q96DB2>).

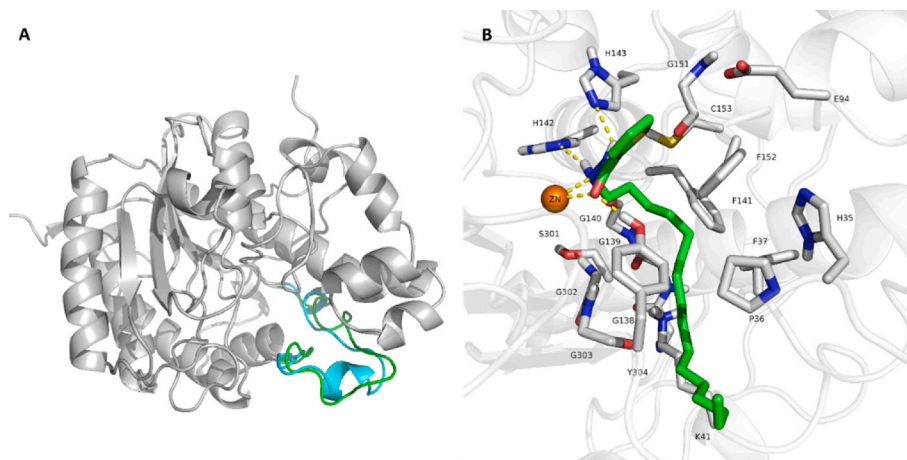


Fig. 9. Remodeling loop 1. **A**, cartoon representation of the superposition of the original and the modified model, loop 1 colored cyan and green respectively. **B**, docked pose of SIS17 in the modified loop 1 HDAC11 model. The protein backbone is represented as white cartoon, the interacting binding site residues as grey sticks, zinc ion as orange sphere and the ligands as green sticks. Hydrogen bonds and coordination bonds are represented as yellow dashed lines.

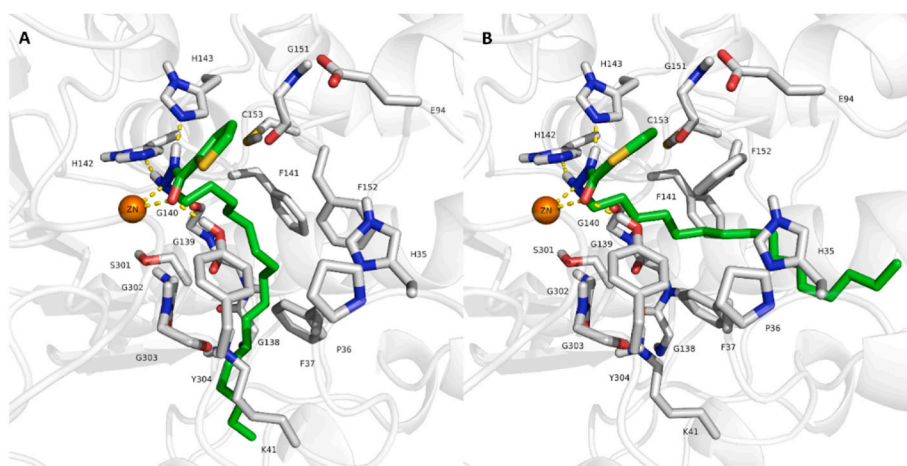


Fig. 10. Docked poses of SIS17. **A** and **B**, are poses with the vertical and horizontal orientation of the alkyl chain, respectively. The protein backbone is represented as white cartoon, the interacting binding site residues as grey sticks, zinc ion as orange sphere and the ligands as green sticks. Hydrogen bonds and coordination bonds are represented as yellow dashed lines.

ligand complex stability and the reliability of the predicted docking poses [34,71]. The initially obtained ligand HDAC11 model complexes which were obtained by transplanting the respective ligand coordinates from HDAC8 crystal structures as well as the selected docked poses were subjected to molecular dynamics simulation to examine the stability of the model after performing the optimization as well as the stability of the obtained ligand poses.

For all the molecular dynamics simulations the RMSD plots shows that the protein is stabilizing between 1 Å and 2 Å, while the zinc ion is stabilizing at around or below 1 Å (Fig. S6, S7, S20, S21, S31 and S36).

3.4.1. Minimized complexes

The bidentate chelation mode was monitored through the stability of the distances between the zinc ion and chelator atoms in the zinc binding group during the molecular dynamics simulations and could be confirmed for the four protein-ligand complexes (Figs. S9 and S10).

Ligand RMSD shows that Trapoxin A and TSA are both stabilizing at about 3 Å (Fig. 11A and B) but with few extreme fluctuations for TSA especially in the first and third run. The RMSD of the first pose of Quisinostat is high reaching up to 6 Å (Fig. 11C) and less repeatable between the three runs with fluctuations over simulation time, while the second pose is showing different behavior in which the ligand is stabilizing at

around 2 Å and repeatability could be observed for the three runs (Fig. 11D).

Trapoxin A hydrogen bonding to His142 or His143 showed moderate to high stability with occupancy ranging between 44 % and 75 % for the three runs (Table S2, Figs. S14 and S15). The occupancy percent of the hydrogen bond to Tyr304 is repeatable for two runs with almost 100 % for the second and third runs, while for the first run the occupancy is as low as 46 %. Hydrogen bonds between the three NH groups of the macrocycle of Trapoxin A and the side chain oxygens of Glu94 are highly stable and showing persistence above 83 % almost for all the three bonds in the three runs.

The salt bridge and the hydrogen bond to His142 and His143, respectively, for both poses of Quisinostat are stable with persistence ranging between 76 and 100 % (Tables S3 and S4, Fig. S11, S12 and S13). For the first pose the hydrogen bond to Tyr304 is showing weak stability or almost completely lost, while in the second pose, the first and third runs demonstrate good stability of hydrogen bond to Tyr304 with occupancy of 80 and 70 % respectively, but almost completely lost for the second run. For the first pose of Quisinostat the overall persistence of the salt bridge to Glu94 is average with occupancy between 50 % and 75 % considering both side chain and backbone interactions. In the second pose and during the simulation, a salt bridge which was not observed in

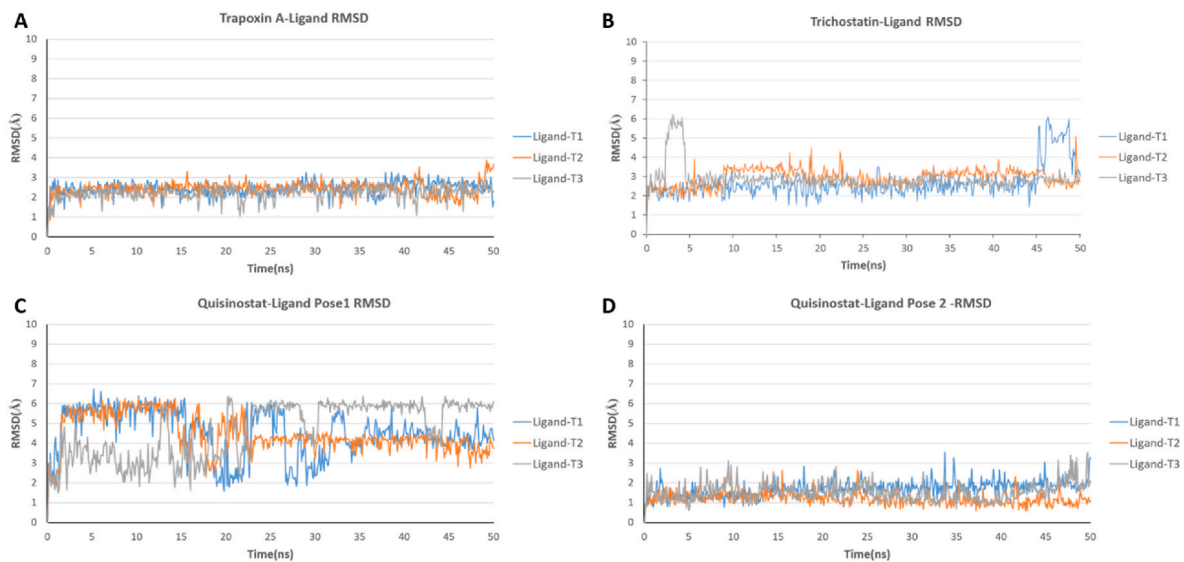


Fig. 11. RMSD plots of ligand heavy atoms for 3 repeated MD runs each for 50 ns. **A**, minimized pose of Trapoxin A. **B**, minimized pose of TSA. **C**, first minimized pose of Quisinostat. **D**, second minimized pose of Quisinostat.

the initial merged and minimized pose between the NH group of the linker and Glu94 was established and showing high stability between 80 % and 91 % for the three runs.

For TSA, the salt bridge to His142 is highly persistent with almost

100 % for all three runs while for the hydrogen bond to His143, weak to average persistence between 27 % and 55 % is observed (Table S5, Figs. S14 and S16). The persistence percent of hydrogen bond to Tyr304 is varied strongly between the three runs between high and average

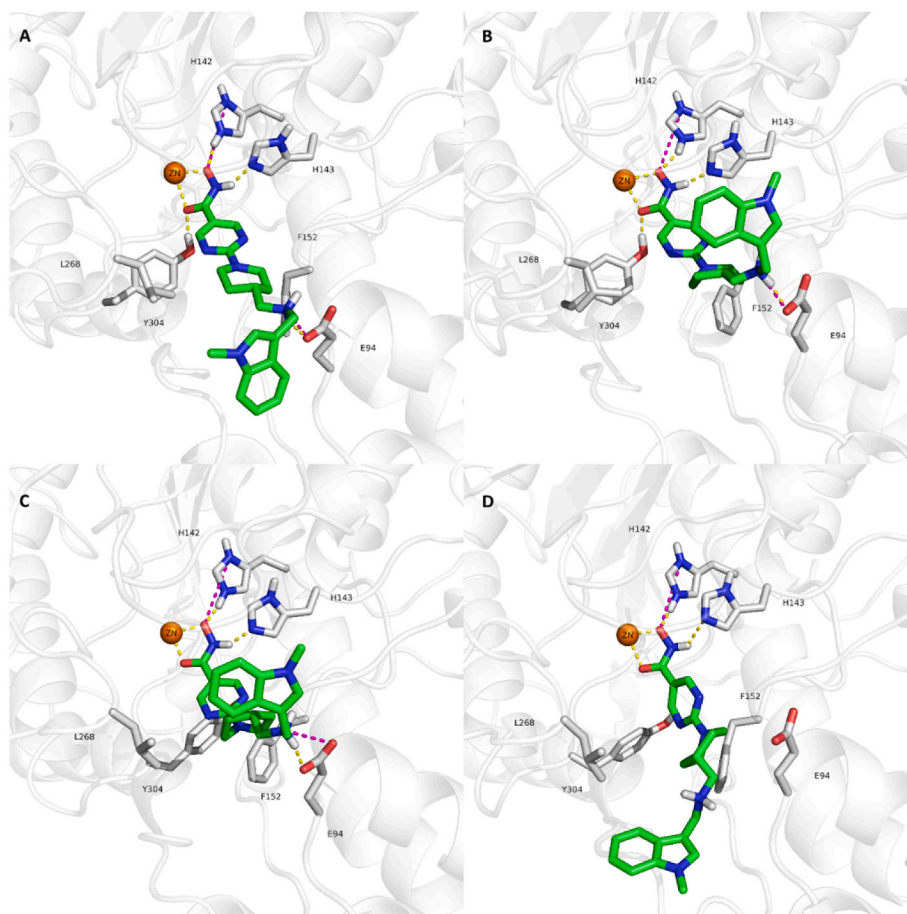


Fig. 12. Selected snapshots from the first MD run of the first pose of Quisinostat showing the fluctuation of the methyl indole capping group. **A**, frame 1. **B**, frame 125. **C**, frame 250. **D**, frame 500. The protein backbone is represented as white cartoon, the interacting binding site residues as grey sticks, zinc ion as orange sphere and the ligands as green sticks. Hydrogen bonds and coordination bonds are represented as yellow dashed lines and the ionic interactions as magenta dashed lines.

persistence or even almost lost completely.

Analyzing the RMSF plots for Trapoxin A shows that the most fluctuating part of the ligand is a terminal phenyl ring that is exposed to the solvent (Figs. S8A and S18). For Quisinostat pose 1, the methyl indole capping group is the most fluctuating substructure of the ligand while in pose 2 the fluctuation of the ligand is below 2 Å (Fig. 12, S8C, S8D and S17). While this fluctuation disturbs the salt bridge to Glu94 that was initially observed in the first pose leading to the demonstrated lower stability, the slight movement of the capping group allows for the formation of the same salt bridge in the second pose during the simulation. The high fluctuation of this part of the ligand reaching up to 6 Å, is responsible mostly for the high RMSD observed in the first pose. The capping group of TSA also show higher RMSF value (Figs. S8B and S19) indicating that it is responsible for the few fluctuations in the RMSD observed in runs one and three.

Analysis of the results of the hydrogen bond persistence of the zinc binding group presented above, shows that the hydrogen bond interaction to Tyr304 is less stable or almost completely lost in some MD runs especially for TSA and both poses of quisinostat. It is worth noting that this conserved tyrosine residue can adopt different conformations in HDACs crystal structures (HDAC8 PDB: 3SFF and 3SFH, HDAC2 PDB: 7KBH) [72,73] which reflects its flexibility. We observed this flexibility also in previously reported MD simulations of available HDAC X-ray structures [74].

3.4.2. Docked hydroxamic acid inhibitors

3.4.2.1. FT895. Examining the results obtained from the short time scale molecular dynamics simulations (50 ns) demonstrates that the RMSD of the docked pose of FT895 is stabilizing at 2 Å (Fig. 13A). Furthermore, the interaction persistence results reveal that the salt bridge stability to His142 is very high with persistence of almost 100 % for all the runs (Table S6, Fig. S26 and S29). The Hydrogen bond to His143 shows moderate to good persistence between 59 % and 88 %, and the stability of the hydrogen bond to Tyr304 was not confirmed.

Extra hydrogen bond between one nitrogen atom in the pyrazine ring in the capping group of FT895 and His183 that was not observed in the initial docked pose was established during the simulation and showed persistence between 63 % and 78 % in the three runs.

The RMSF plot for the ligand shows that all FT895 atoms are fluctuating at around 1 Å (Fig. S22A) thus indicating for the high stability observed in the RMSD. The bidentate chelation was confirmed by monitoring the stability of the distances between the zinc ion and the chelator atoms of the hydroxamate moiety except for few sharp fluctuations for the distance between the zinc ion and the carbonyl oxygen. (Figs. S23A and S24A).

The RMSD resulted from the longer molecular dynamics simulation (500 ns) shows that FT895 is stabilizing at around 2 Å for about 250 ns after which a slight shift in the pose causing the RMSD to reach 4 Å was observed (Fig. 13B and S27B). Analyzing the RMSF of the ligand atoms revealed that only the trifluoromethylpyrazine shows slight fluctuations, however the RMSF values still remain below 2.2 Å (Fig. 14 and

S22A), indicating that no major shifts occurred during the MD-simulation. Additionally, the observed ligand-protein interactions remained stable throughout the simulation; the bidentate chelation mode of the zinc ion was maintained (Fig. S25A), and the salt bridge and hydrogen bond interactions to His142, His143 and His183 remained stable with persistence of 99 %, 80 % and 58 %, respectively (Figs. S27A and S29).

Overall, the predicted binding mode of FT895 in HDAC11 showed good stability during the long MD simulation and the key interactions were preserved, despite the slight shift in the position of the capping group.

3.4.2.2. MIR002. For MIR002, the RMSD plot shows that the ligand is stabilizing at about 3 Å (Fig. 15A) and the salt bridge stability to His142 was confirmed showing almost 100 % persistence for all three runs (Table S7, Fig. S26 and S30). More fluctuation of the persistence percent between the three runs for the hydrogen bond to His143 and Tyr304 was observed ranging between 34 % to 71 % and 50 %–81 %, respectively.

For MIR002 the most fluctuating part is the cinnamic acid capping group that is exposed to the solvent reaching up to 3 Å (Fig. S22B). The starting distance between the carbonyl oxygen and the zinc ion observed in the docked pose of 2.84 Å was adjusted during the simulation to below the threshold of 2.6 Å. The stability of the bidentate chelation mode can be confirmed as the distances between the zinc ion and the chelator atoms of the zinc binding group are stable, however, few sharp fluctuations can also be observed for the carbonyl oxygen (Figs. S23B and S24B).

Long molecular dynamics simulation on the predicted binding mode of MIR002 showed similar behavior as compared to the shorter runs with the RMSD of the ligand stabilizing at around 3 Å (Fig. 15B). The highest fluctuations were observed for the cinnamic acid moiety of the capping group with RMSF reaching 3 Å (Fig. 16, S22B and S28B).

Analysis of the protein ligand interactions shows that the salt bridge and hydrogen bond interactions to His142 and His143, respectively, are maintained with persistence of 99 % and 62 %, respectively. (Figs. S28A and S30). Additionally, the bidentate chelation of the zinc is majorly preserved as confirmed by monitoring the distance between the zinc ion and the chelator atoms of the hydroxamate moiety (Fig. S25B).

3.4.3. Docked alkyl hydrazide inhibitors

3.4.3.1. Loop1-remodeled pose. Inspecting the results from the molecular dynamics simulation for the docked pose of SIS17 in the loop 1 remodeled HDAC11, shows that SIS17 is stabilizing between 2 Å and 3 Å all over the simulation and for the three replica except for the third simulation as a raise of the RMSD reaching 5 Å can be observed by the end of the simulation (Fig. 17). Repeating this third run starting from the same seed but for longer duration of 100 ns could confirm the observation that there is a shift in the initially obtained pose leading the RMSD to fluctuate to such higher values of 5 Å to 7 Å starting from around 50 ns till the end of the simulation.

The hydrogen bonds stability to His142 and His143 was confirmed

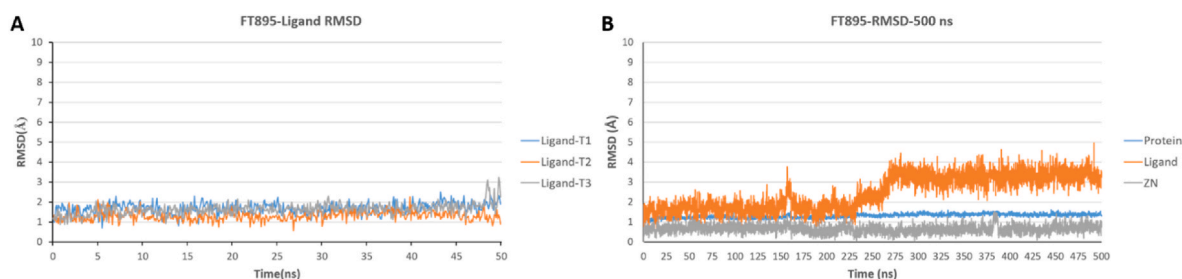


Fig. 13. FT895 RMSD. **A**, RMSD plots of ligand heavy atoms for 3 repeated MD simulation each for 50 ns. **B**, RMSD plot of protein backbone heavy atoms, zinc ion and ligand heavy atoms for 500 ns MD simulation.

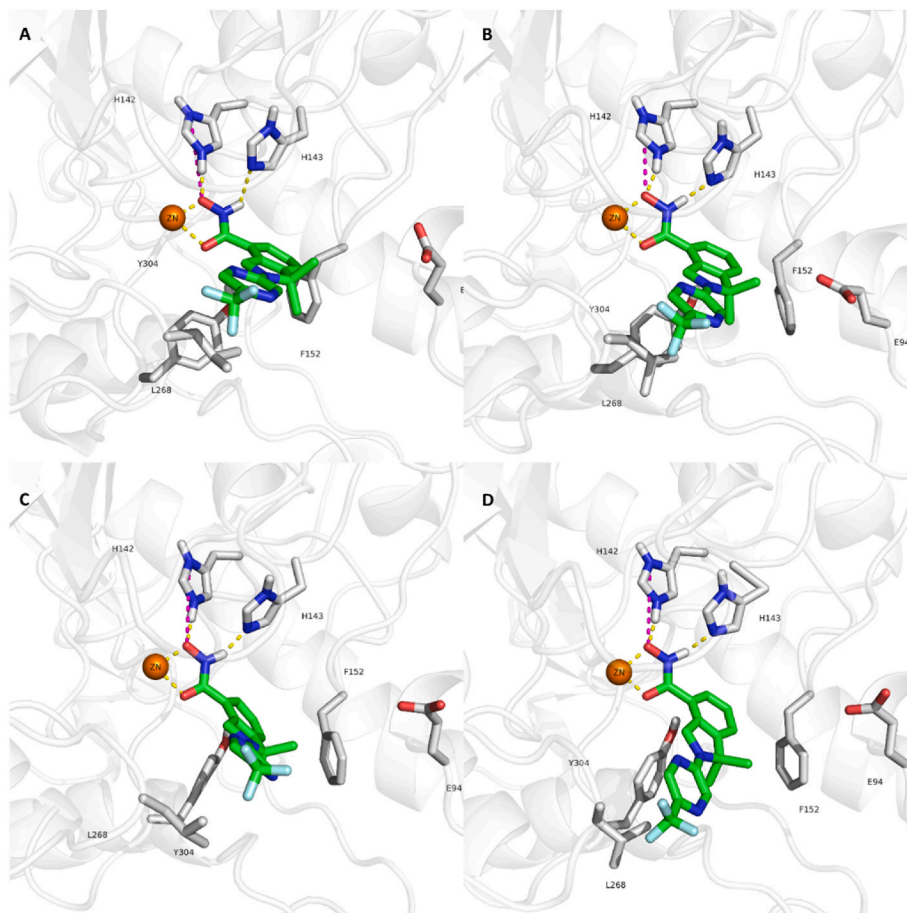


Fig. 14. Selected snapshots from the long MD run (500 ns) of FT895 showing the fluctuation of the trifluoromethylpyrazine capping group and the slight shift in the pose. **A**, frame 1. **B**, frame 1250. **C**, frame 2500. **D**, frame 5000. The protein backbone is represented as white cartoon, the interacting binding site residues as grey sticks, zinc ion as orange sphere and the ligands as green sticks. Hydrogen bonds and coordination bonds are represented as yellow dashed lines and the ionic interactions as magenta dashed lines.

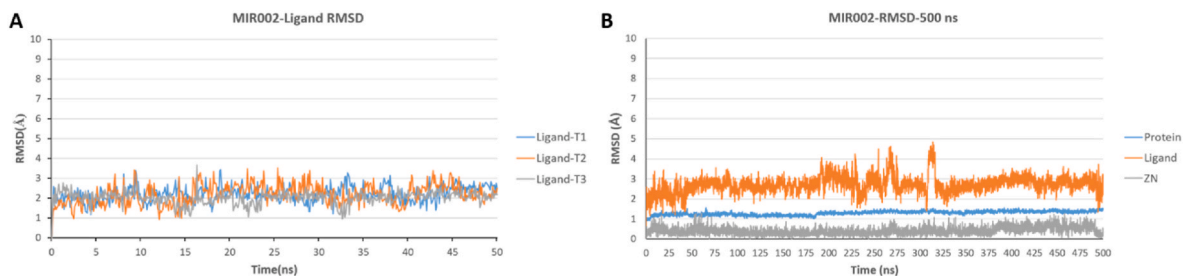


Fig. 15. MIR002 RMSD. **A**, RMSD plots of ligand heavy atoms for 3 repeated MD simulation each for 50 ns. **B**, RMSD plot of protein backbone heavy atoms, zinc ion and ligand heavy atoms for 500 ns MD simulation.

with persistence ranging between 73 % and 100 % (Table S10, Fig. S33, S34 and S35) indicating that this shift in the pose observed is not affecting interactions of the zinc binding group. The RMSF of the repeated longer run indicates that the most fluctuating part of the ligand is the distal part of the long alkyl chain (Fig. S32). By inspecting the trajectory frames, a shift of the alkyl chain from its initial docked pose that is accommodated between loop 1 and loop 7 to a different direction ending up resting between loop 1 and loop 2 was observed.

3.4.3.2. Stepwise docking and minimization poses. The RMSD and the RMSF plots of SIS17 in both the horizontal and the vertical poses indicate stable poses that reflects the probability of the long alkyl chain being conveniently accommodated within either direction (Fig. 18 and

S37). The ligand in both poses is stabilizing below 3 Å. The ligand RMSF in the vertical pose is less than 2 Å for all ligand atoms, while the terminal part of the alkyl chain is showing slightly higher fluctuation for the horizontal pose.

The hydrogen bond stability is comparable between both poses. The hydrogen bond persistence to His142 and His143 is above 90 % for all runs, while for Tyr304 the hydrogen bond is almost completely lost (Tables S8 and S9, Figs. S38–S40 and S42).

Superposing the structures of HDAC11 AlphaFold model, HDAC6 and HDAC8 shows that the folding of loop 3 is more homologous to HDAC8 than to HDAC6 which can be expected due to higher similarity of this region to HDAC8 than to HDAC6 (Fig. 19). In HDAC8 and the AlphaFold model of HDAC11 three similar residues of Gly139, Gly140

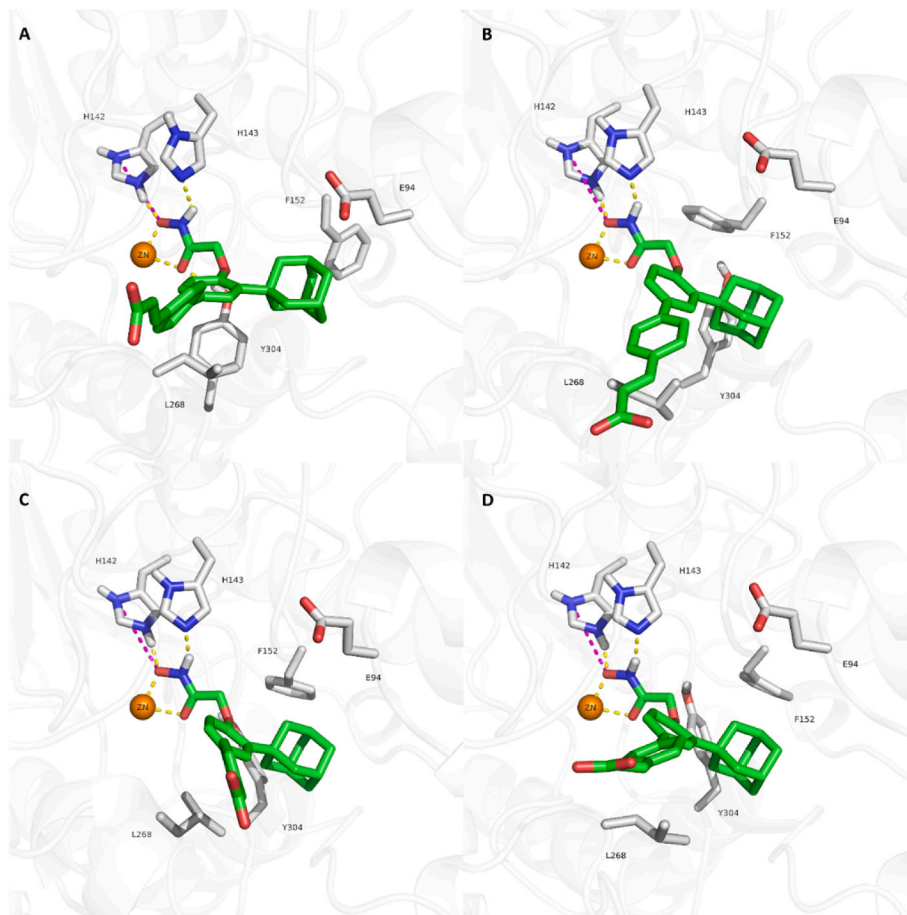


Fig. 16. Selected snapshots from the long MD run (500 ns) of MIR002 showing the fluctuation of the cinnamic acid capping group. **A**, frame 1. **B**, frame 1250. **C**, frame 2500. **D**, frame 5000. The protein backbone is represented as white cartoon, the interacting binding site residues as grey sticks, zinc ion as orange sphere and the ligands as green sticks. Hydrogen bonds and coordination bonds are represented as yellow dashed lines and the ionic interactions as magenta dashed lines.

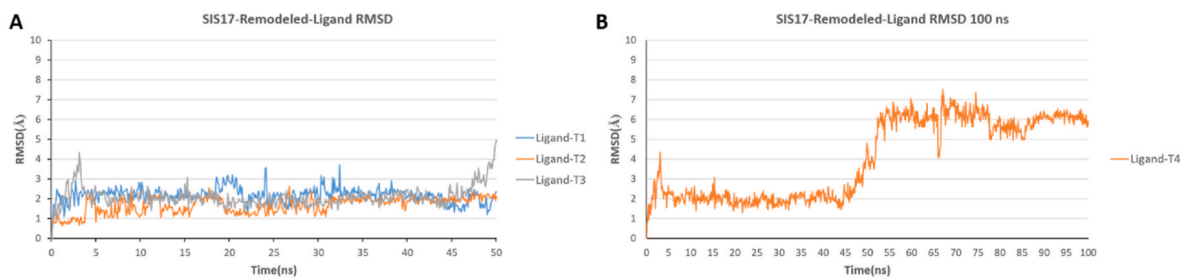


Fig. 17. RMSD plots of ligand heavy atoms for SIS17 in the loop 1 remodeled HDAC11. **A**, 3 repeated MD runs each for 50 ns. **B**, repeated third run for 100 ns.

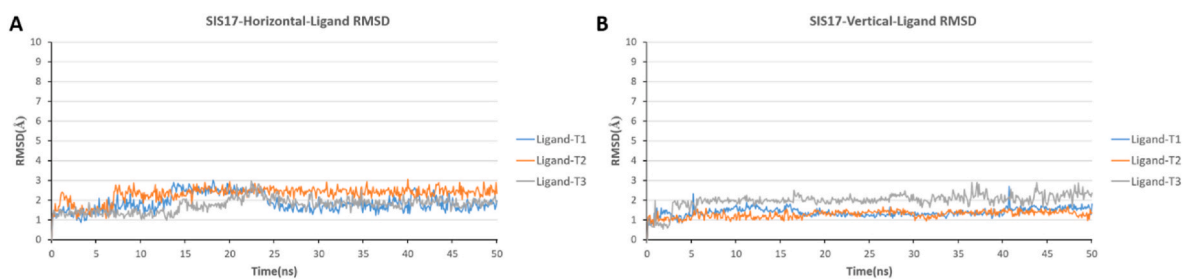


Fig. 18. RMSD plots of ligand heavy atoms for 3 repeated MD runs each for 50 ns. **A** and **B**, the horizontal and vertical poses of SIS17, respectively.

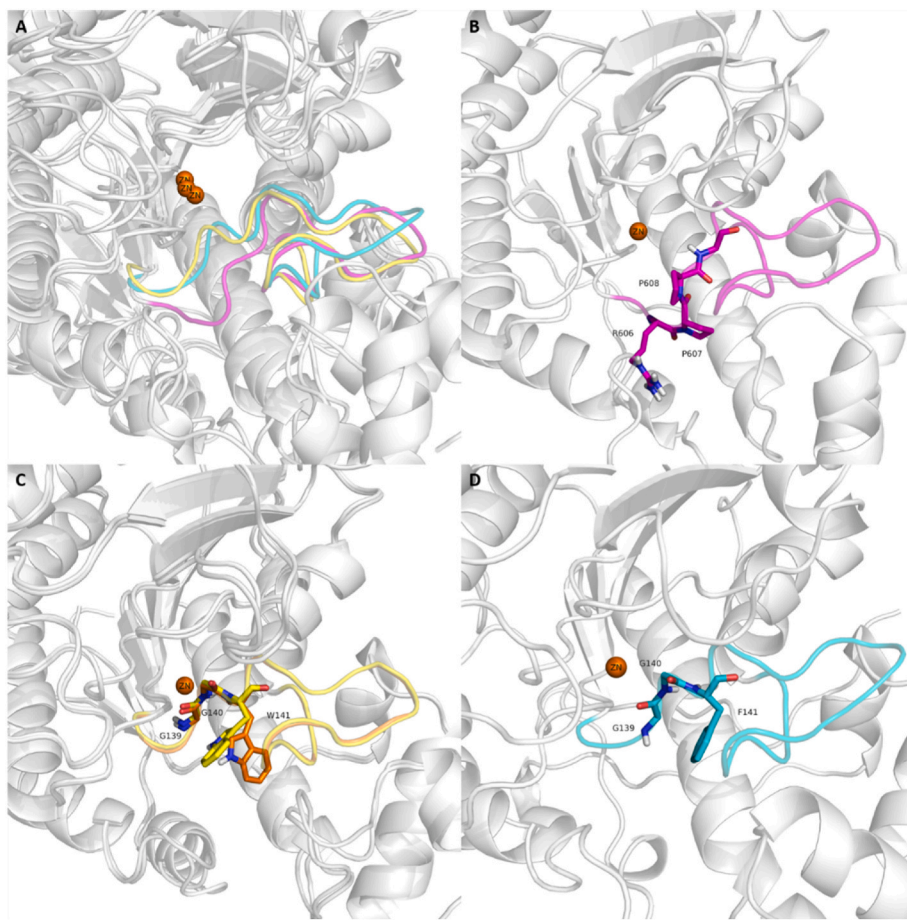


Fig. 19. Loop 3 comparison between HDAC6, HDAC8 and HDAC 11 AlphaFold model. Protein backbone is represented as white cartoon and zinc as orange sphere. **A,** Superposition of HDAC6 PDB 5EDU, HDAC8 PDB 5FCW and HDAC11 AlphaFold model. Loop 3 colored as magenta, yellow and cyan for HDAC6, HDAC8 and HDAC11 respectively. **B,** HDAC6 PDB 5EDU, loop 3 residues represented as magenta sticks. **C,** Superposition of 2 HDAC8 crystal structures showing the flexibility of the gate keeper Trp141. Loop 3 residues are colored yellow and orange for 5FCW and 6ODC, respectively. **D,** HDAC11 AlphaFold model, loop 3 residues represented as cyan sticks.

and Trp141 in HDAC8 and Phe141 in HDAC11 are shaping the entrance of what so called foot pocket and the flexible Trp141 and Phe141 side chains are acting as the gate keeper residues. These three residues are replaced by Arg606, Pro607 and Pro608 in HDAC6. The bulkier non-flexible side chains of Pro607 and Pro608 along with the bulky side chain of Arg606 that is directed towards loop 1 to form polar interactions with Glu502 [21] are causing this part of the loop to fold into the opposite direction thus blocking the space required for the formation

of the foot pocket.

Since HDAC8 is also well known for the deacylase activity [75] this observed similarity can suggest the pose of SIS17 with its alkyl chain directed vertically into the binding pocket along loop 3 and loop 7 to be the most reasonable pose for SIS17.

As the vertical pose was considered the most reasonable pose regarding the orientation of the alkyl chain of SIS17, longer molecular dynamics simulation run of 500 ns was also performed. The RMSD of the

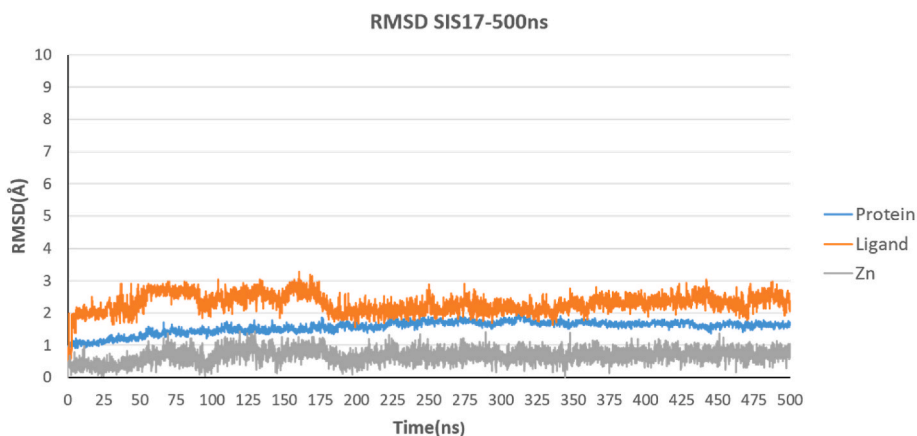


Fig. 20. SIS17 vertical pose RMSD plot of protein backbone heavy atoms, zinc ion and ligand heavy atoms for 500 ns MD simulation.

ligand is stabilizing between 2 Å and 3 Å (Fig. 20) and the hydrogen bond stability to His142 and His143 was confirmed with persistence of about 99 % and 92 %, respectively (Figs. S41A and S42).

The RMSF of the ligand showed that the long alkyl chain is fluctuating more than observed in the shorter runs however, still below 2 Å (Fig. 21, S37A and S41B).

4. Conclusion

In this study, the HDAC11 AlphaFold model was successfully optimized by adding and adjusting the coordination of the zinc ion. Furthermore the binding site was optimized by minimizations in presence of different inhibitors resulting in four protein ligand complexes. The stability of the protein and the binding mode in terms of the hydrogen bond pattern and metal chelation observed after the minimization was confirmed by molecular dynamics simulation for these four complexes which reflects the validity of the optimization process and usability of the obtained optimized complexes for the next step.

Utilization of the obtained complexes of the optimized model to generate grids for docking of selective inhibitors was successful and supported by molecular dynamics simulation that confirmed the stability of the obtained poses and their initial observed interactions.

Furthermore, the selective HDAC11 inhibitor SIS17 was used to explore the foot pocket using different approaches including a stepwise docking and minimization process as well as direct docking in loop 1 modified model. The two approaches resulted in docked poses of SIS17 with three different orientations, identifying three different tunnels as possible foot pocket that can accommodate such long alkyl chain,

however the docking solution that is placing the alkyl chain deeper into the protein along loop 3 and loop 7 was considered the most reasonable.

Considering the results obtained from this study along with inspecting the transplants from AlphaFill indicate that the AlphaFill approach was not successful in obtaining optimal complexes in terms of zinc coordination and clash free inhibitor poses. This can be understandable knowing that AlphaFill is using a sequence and structure similarity approach for searching for homologous templates for alignment and small molecule transplantation and suggesting that AlphaFill would be more successful with protein sequence showing higher similarity and identity percent with crystal structures available in the protein data bank which is not observed for HDAC11.

As a conclusion, for the aim of drug design and inhibitor optimization, whenever there is reliable identity and similarity percent for the protein sequence of interest with available experimentally determined structures, the conventional template based homology modeling in presence of ligands and cofactors is recommended. The current study also showed that the models obtained from the AlphaFold approach can still be utilized but with caution. The main aim of our study was to develop a suitable 3D model of the studied target protein (HDAC11) using previously reported inhibitors and assessing its usability for drug design studies. Nevertheless, some limitations of the herein used *in silico* drug design methodologies have to be put into consideration. The nanoscale time scale of classical MD simulation limits the possibility to study several biological events including larger conformational changes observed for ligand binding and unbinding processes. Moreover, since classical MD simulations uses molecular mechanics force fields, only potential energies are considered whereas entropic contributions are

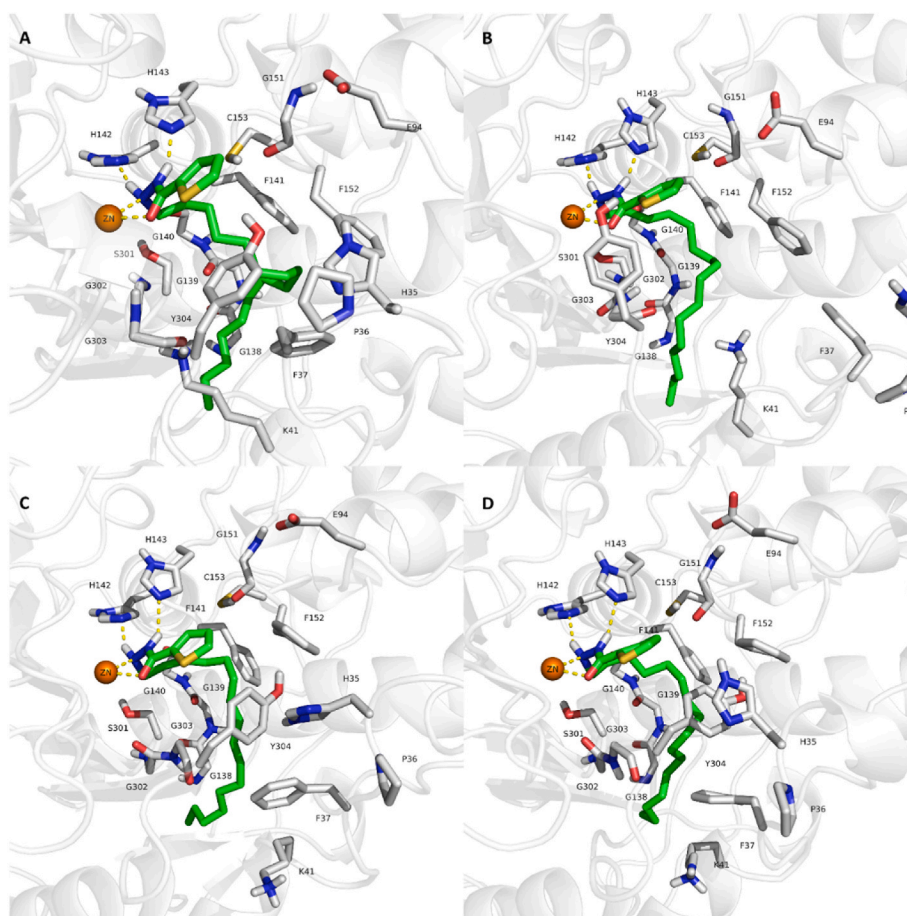


Fig. 21. Selected snapshots from the long MD run (500 ns) of SIS17 showing the fluctuation of the long alkyl chain. **A**, frame 1. **B**, frame 1250. **C**, frame 2500. **D**, frame 5000. The protein backbone is represented as white cartoon, the interacting binding site residues as grey sticks, zinc ion as orange sphere and the ligands as green sticks. Hydrogen bonds and coordination bonds are represented as yellow dashed lines.

neglected. Therefore, only the enthalpic part of the ligand binding is calculated usually. Another general limitation of the working with homology models is the lacking of water molecules that might affect the ligand and the stability of the interactions during the simulation. Verification through experimental 3D structure determination or design and evaluation of ligands based on the presented model is still required for further confirmation of the generated models.

Author contributions

FB and DR did the computational studies and wrote the manuscript. WS supervised the experiments and revised the manuscript.

Declaration of competing interest

The authors declare that they have no known competing financial interests or personal relationships that could have appeared to influence the work reported in this paper.

Appendix A. Supplementary data

Supplementary data to this article can be found online at <https://doi.org/10.1016/j.combiomed.2023.107700>.

References

- S.S. Liu, F. Wu, Y.M. Jin, W.Q. Chang, T.M. Xu, HDAC11: a rising star in epigenetics, *Biomed. Pharmacother.* (2020) 131.
- L. Gao, M.A. Cueto, F. Asselbergs, P. Atadja, Cloning and functional characterization of HDAC11, a novel member of the human histone deacetylase family, *J. Biol. Chem.* 277 (28) (2002) 25748–25755.
- T.A. Boltz, S. Khuri, S. Wuchty, Promoter conservation in HDACs points to functional implications, *BMC Genom.* 20 (1) (2019).
- M. Lundh, D.P. Christensen, D.N. Rasmussen, P. Mascagni, C.A. Dinarello, N. Billestrup, L.G. Grunnet, T. Mandrup-Poulsen, Lysine deacetylases are produced in pancreatic beta cells and are differentially regulated by proinflammatory cytokines, *Diabetologia* 53 (12) (2010) 2569–2578.
- F. Cheng, M. Lienlaf, P. Perez-Villarreal, H.W. Wang, C. Lee, K. Woan, D. Woods, T. Knox, J. Bergman, J. Pinilla-Ibarz, A. Kozikowski, E. Seto, E.M. Sotomayor, A. Villagra, Divergent roles of histone deacetylase 6 (HDAC6) and histone deacetylase 11 (HDAC11) on the transcriptional regulation of IL10 in antigen presenting cells, *Mol. Immunol.* 60 (1) (2014) 44–53.
- C. Yanginlar, C. Logie, HDAC11 is a regulator of diverse immune functions, *Biochim Biophys Acta - Gene Regul Mech.* 1861 (1) (2018) 54–59.
- A. Villagra, F. Cheng, H.W. Wang, I. Suarez, M. Glozak, M. Maurin, D. Nguyen, K. L. Wright, P.W. Atadja, K. Bhalla, J. Pinilla-Ibarz, E. Seto, E.M. Sotomayor, The histone deacetylase HDAC11 regulates the expression of interleukin 10 and immune tolerance, *Nat. Immunol.* 10 (1) (2009) 92–100.
- H. Yang, J. Yang, H. Cheng, H. Cao, S. Tang, Q. Wang, J. Zhao, B. Li, Y. Ding, C. Ma, Probiotics ingestion prevents HDAC11-induced DEC205+ dendritic cell dysfunction in night shift nurses, *Sci. Rep.* 9 (1) (2019).
- J. Cao, L. Sun, P. Aramsangtienchai, N.A. Spiegelman, X. Zhang, W. Huang, E. Seto, H. Lin, HDAC11 regulates type I interferon signaling through defatty-acylation of SHMT2, *Proc. Natl. Acad. Sci. U.S.A.* 116 (12) (2019) 5487–5492.
- L. Sun, C. Marin de Evsikova, K. Bian, A. Achille, E. Telles, H. Pei, E. Seto, Programming and regulation of metabolic homeostasis by HDAC11, *EBioMedicine* 33 (2018) 157–168.
- R.A. Bagchi, B.S. Ferguson, M.S. Stratton, T. Hu, M.A. Cavasin, L. Sun, Y.H. Lin, D. Liu, P. Londono, K. Song, M.F. Pino, L.M. Sparks, S.R. Smith, P.E. Scherer, S. Collins, E. Seto, T.A. McKinsey, HDAC11 suppresses the thermogenic program of adipose tissue via BRD2, *JCI insight* 3 (15) (2018 Aug 9).
- W. Wang, B. Ding, W. Lou, S. Lin, Promoter hypomethylation and miR-145-5p downregulation-mediated HDAC11 overexpression promotes sorafenib resistance and metastasis of hepatocellular carcinoma cells, *Front. Cell Dev. Biol.* 8 (2020).
- Q. Fei, F. Song, X. Jiang, H. Hong, X. Xu, Z. Jin, X. Zhu, B. Dai, J. Yang, C. Sui, M. Xu, LncRNA ST8SIA6-AS1 promotes hepatocellular carcinoma cell proliferation and resistance to apoptosis by targeting miR-4656/HDAC11 axis, *Cancer Cell Int.* 20 (1) (2020).
- K. Freese, T. Seitz, P. Dietrich, S.M.L. Lee, W.E. Thasler, A. Bosserhoff, C. Hellerbrand, Histone deacetylase expressions in hepatocellular carcinoma and functional effects of histone deacetylase inhibitors on liver cancer cells in vitro, *Cancers* 11 (10) (2019).
- D. Gong, Z. Zeng, F. Yi, J. Wu, Inhibition of histone deacetylase 11 promotes human liver cancer cell apoptosis, *Am. J. Transl. Res.* 11 (2) (2019) 983–990.
- W. Huo, F. Qi, K. Wang, Long non-coding RNA BCYRN1 promotes prostate cancer progression via elevation of HDAC11, *Oncol. Rep.* 44 (3) (2020 Jul 7) 1233–1245.
- W. Wang, L. Fu, S. Li, Z. Xu, X. Li, Histone deacetylase 11 suppresses p53 expression in pituitary tumor cells, *Cell Biol. Int.* 41 (12) (2017) 1290–1295.
- L. Yue, V. Sharma, N.P. Horvat, A.A. Akuffo, M.S. Beatty, C. Murdun, C. Colin, J.M. R. Billington, W.E. Goodheart, E. Sahakian, L. Zhang, J.J. Powers, N.E. Amin, Q. T. Lambert-Showers, L.N. Darville, J. Pinilla-Ibarz, G.W. Reuther, K.L. Wright, C. Conti, J.Y. Lee, X. Zheng, P.Y. Ng, M.W. Martin, C.G. Marshall, J.M. Koomen, R. L. Levine, A. Verma, H.L. Grimes, E.M. Sotomayor, Z. Shao, P.K. Epling-Burnette, HDAC11 deficiency disrupts oncogene-induced hematopoiesis in myeloproliferative neoplasms, *Blood* 135 (3) (2020) 191–207.
- S. Mithraprabhu, A. Kalff, A. Chow, T. Khong, A. Spencer, Dysregulated Class I histone deacetylases are indicators of poor prognosis in multiple myeloma, *Epigenetics* 9 (11) (2014 Nov 2) 1511–1520.
- T.M. Thole, M. Lodrini, J. Fabian, J. Wuenschel, S. Pfeil, T. Hielscher, A. Kopp-Schneider, U. Heinicke, S. Fulda, O. Witt, A. Eggert, M. Fischer, H.E. Deubzer, Neuroblastoma cells depend on HDAC11 for mitotic cell cycle progression and survival, *Cell Death Dis.* 8 (3) (2017).
- Z. Kutil, Z. Novakova, M. Meleshin, J. Mikesova, M. Schutkowski, C. Barinka, Histone deacetylase 11 is a fatty-acid deacylase, *ACS Chem. Biol.* 13 (3) (2018 Mar 16) 685–693.
- C. Moreno-Yruela, I. Galleano, A.S. Madsen, C.A. Olsen, Histone deacetylase 11 is an e-N-methyllysine hydrolase, *Cell Chem. Biol.* 25 (7) (2018 Jul), 849–856.e8.
- Z. Kutil, J. Mikesová, M. Zessin, M. Meleshin, Z. Nováková, G. Alquicer, A. Kozikowski, W. Sippl, C. Barinka, M. Schutkowski, Continuous activity assay for HDAC11 enabling reevaluation of HDAC inhibitors, *ACS Omega* 4 (22) (2019) 19895–19904.
- Y. Chen, X. Wang, W. Xiang, L. He, M. Tang, F. Wang, T. Wang, Z. Yang, Y. Yi, H. Wang, T. Niu, L. Zheng, L. Lei, X. Li, H. Song, L. Chen, Development of purine-based hydroxamic acid derivatives: potent histone deacetylase inhibitors with marked in vitro and in vivo antitumor activities, *J. Med. Chem.* 59 (11) (2016 Jun 9) 5488–5504.
- J. Arts, P. King, A. Mariën, W. Floren, A. Beliën, L. Janssen, I. Pilatte, B. Roux, L. Decrane, R. Gilissen, I. Hickson, V. Vreys, E. Cox, K. Bol, W. Talloen, I. Goris, L. Andries, M. Du Jardin, M. Janicot, M. Page, K. Van Emelen, P. Angibaud, JNJ-26481585, a novel “second-generation” oral histone deacetylase inhibitor, shows broad-spectrum preclinical antitumoral activity, *Clin. Cancer Res.* 15 (22) (2009 Nov 15) 6841–6851.
- C.W. Yu, P.T. Chang, L.W. Hsin, J.W. Chern, Quinazolin-4-one derivatives as selective histone deacetylase-6 inhibitors for the treatment of Alzheimer’s disease, *J. Med. Chem.* 56 (17) (2013 Sep 12) 6775–6791.
- M.W. Martin, J.Y. Lee, D.R. Lancia, P.Y. Ng, B. Han, J.R. Thomason, M.S. Lynes, C. G. Marshall, C. Conti, A. Collis, M.A. Morales, K. Doshi, A. Rudnitskaya, L. Yao, X. Zheng, Discovery of novel N-hydroxy-2-arylsindoline-4-carboxamides as potent and selective inhibitors of HDAC11, *Bioorg. Med. Chem. Lett* 28 (12) (2018) 2143–2147.
- S.I. Son, J. Cao, C.L. Zhu, S.P. Miller, H. Lin, Activity-guided design of HDAC11-specific inhibitors, *ACS Chem. Biol.* 14 (7) (2019) 1393–1397.
- T.T. Ho, C. Peng, E. Seto, H. Lin, Trapoxin A analogue as a selective nanomolar inhibitor of HDAC11, *ACS Chem. Biol.* 18 (4) (2023) 803–809.
- S. Dallavalle, L. Musso, R. Cincinelli, N. Darwiche, S. Gervasoni, G. Vistoli, M. B. Guglielmi, I. La Porta, M. Pizzulo, E. Modica, F. Prospero, G. Signorino, F. Colelli, F. Cardile, A. Fucci, E.L. D’Andrea, A. Riccio, C. Pisano, Antitumor activity of novel POLA1-HDAC11 dual inhibitors, *Eur. J. Med. Chem.* (2022) 228.
- F.D. Prieto-Martínez, E. López-López, K. Eurrídice Juárez-Mercado, J.L. Medina-Franco, Computational drug design methods—current and future perspectives, in: *Silico Drug Design: Repurposing Techniques and Methodologies*, Elsevier, 2019, pp. 19–44.
- V.T. Sabe, T. Ntombela, L.A. Jhamba, G.E.M. Maguire, T. Govender, T. Naicker, H. G. Kruger, Current trends in computer aided drug design and a highlight of drugs discovered via computational techniques: a review, *Eur. J. Med. Chem.* 224 (2021 Nov), 113705.
- C. Athanasiou, Z. Cournia, From computers to bedside: computational Chemistry contributing to FDA approval, in: *Biomolecular Simulations in Structure-Based Drug Discovery*, 2018, pp. 163–203.
- T.I. Adelusi, A.Q.K. Oyedele, I.D. Boyenle, A.T. Ogunlana, R.O. Adeyemi, C. D. Ukachi, M.O. Idris, O.T. Olaoba, I.O. Adedotun, O.E. Kolawole, Y. Xiaoxing, M. Abdul-Hammed, Molecular modeling in drug discovery, *Inform. Med. Unlocked* 29 (2022), 100880.
- J. Jumper, R. Evans, A. Pritzel, T. Green, M. Figurnov, O. Ronneberger, K. Tunyasuvunakool, R. Bates, A. Židek, A. Potapenko, A. Bridgland, C. Meyer, S.A. Kohl, A.J. Ballard, A. Cowie, B. Romera-Paredes, S. Nikolov, R. Jain, J. Adler, T. Back, S. Petersen, D. Reiman, E. Clancy, M. Zielinski, M. Steinegger, M. Pacholska, T. Berghammer, S. Bodenstein, D. Silver, O. Vinyals, A.W. Senior, K. Kavukcuoglu, P. Kohli, D. Hassabis, Highly accurate protein structure prediction with AlphaFold, *Nature* 596 (7873) (2021) 583–589.
- A. David, S. Islam, E. Tankhilevich, M.J.E. Sternberg, The AlphaFold database of protein structures: a biologist’s guide, *J. Mol. Biol.* 434 (2) (2022).
- M.L. Hekkelman, I. de Vries, R.P. Joosten, A. Perrakis, AlphaFill: enriching AlphaFold models with ligands and cofactors, *Nat. Methods* 20 (2) (2023) 205–213.
- N.J. Porter, D.W. Christianson, Binding of the microbial cyclic tetrapeptide Trapoxin A to the class I histone deacetylase HDAC8, *ACS Chem. Biol.* 12 (9) (2017) 2281–2286.
- M. Marek, T.B. Shaik, T. Heimburg, A. Chakrabarti, J. Lancelot, E. Ramos-Morales, C. Da Veiga, D. Kalinin, J. Melesina, D. Robaa, K. Schmidt-kunz, T. Suzuki, R. Holl, E. Ennifar, R.J. Pierce, M. Jung, W. Sippl, C. Romier, Characterization of histone deacetylase 8 (HDAC8) selective inhibition reveals specific active site structural and functional determinants, *J. Med. Chem.* 61 (22) (2018) 10000–10016.

- [40] C. Decroos, N.H. Christianson, L.E. Gullett, C.M. Bowman, K.E. Christianson, M. A. Deardorff, D.W. Christianson, Biochemical and structural characterization of HDAC8 mutants associated with cornelia de Lange syndrome spectrum disorders, *Biochemistry* 54 (42) (2015) 6501–6513.
- [41] Schrödinger Release 2019-1, Maestro, Schrödinger, LLC, New York, NY, 2019.
- [42] G. Madhavi Sastry, M. Adzhigirey, T. Day, R. Annabhimoju, W. Sherman, Protein and ligand preparation: parameters, protocols, and influence on virtual screening enrichments, *J. Comput. Aided Mol. Des.* 27 (2013) 221–234.
- [43] Schrödinger Release 2019-1: Protein Preparation Wizard, Epik, Schrödinger, LLC, New York, NY, 2019. Impact, Schrödinger, LLC, New York, NY, 2019; Prime, Schrödinger, LLC, New York, NY, 2019., in.
- [44] J.R. Greenwood, D. Calkins, A.P. Sullivan, J.C. Shelley, Towards the comprehensive, rapid, and accurate prediction of the favorable tautomeric states of drug-like molecules in aqueous solution, *J. Comput. Aided Mol. Des.* 24 (2010) 591–604.
- [45] J.C. Shelley, A. Cholleti, L. Frye, J.R. Greenwood, M.R. Timlin, M. Uchimaya, Epik: a software program for pKa prediction and protonation state generation for drug-like molecules, *J. Comp.-Aided Mol. Design* 21 (2007) 681–691.
- [46] Schrödinger Release 2019-1, Epik, Schrödinger, LLC, New York, NY, 2019.
- [47] E. Harder, W. Damm, J. Maple, C. Wu, M. Reboul, J.Y. Xiang, L. Wang, D. Lupyan, M.K. Dahlgren, J.L. Knight, J.W. Kaus, D.S. Cerutti, G. Krilov, W.L. Jorgensen, R. Abel, R.A. Friesner, OPLS3: a force field providing broad coverage of drug-like small molecules and proteins, *J. Chem. Theor. Comput.* (2015), <https://doi.org/10.1021/acs.jctc.5b00864>.
- [48] D. Shivakumar, J. Williams, Y. Wu, W. Damm, J. Shelley, W. Sherman, Prediction of absolute solvation free energies using molecular dynamics free energy perturbation and the OPLS force field, *J. Chem. Theor. Comput.* 6 (2010) 1509–1519.
- [49] W.L. Jorgensen, D.S. Maxwell, J. Tirado-Rives, Development and testing of the OPLS all-atom force field on conformational energetics and properties of organic liquids, *J. Am. Chem. Soc.* 118 (45) (1996) 11225–11236.
- [50] W.L. Jorgensen, J. Tirado-Rives, The OPLS [optimized potentials for liquid simulations] potential functions for proteins, energy minimizations for crystals of cyclic peptides and crambin, *J. Am. Chem. Soc.* 110 (6) (1988) 1657–1666.
- [51] Schrödinger Release 2019-1, LigPrep, Schrödinger, LLC, New York, NY, 2019.
- [52] M.P. Jacobson, D.L. Pincus, C.S. Rapp, T.J.F. Day, B. Honig, D.E. Shaw, R. A. Friesner, A hierarchical approach to all-atom protein loop prediction, *Proteins: Struct., Funct., Bioinf.* 55 (2004) 351–367.
- [53] M.P. Jacobson, R.A. Friesner, Z. Xiang, B. Honig, On the role of crystal packing forces in determining protein sidechain conformations, *J. Mol. Biol.* 320 (2002) 597–608.
- [54] Schrödinger Release 2019-1: Prime, Schrödinger, LLC, New York, NY, 2019.
- [55] T. Halgren, Identifying and characterizing binding sites and assessing druggability, *J. Chem. Inf. Model.* 49 (2009) 377–389.
- [56] T. Halgren, New method for fast and accurate binding-site identification and analysis, *Chem. Biol. Drug Des.* 69 (2007) 146–148.
- [57] Schrödinger Release 2019-1, SiteMap, Schrödinger, LLC, New York, NY, 2019.
- [58] Kevin J. Bowers, Edmond Chow, Huafeng Xu, O. Ron, Michael P. Eastwood Dror, Brent A. Gregersen, John L. Klepeis, Istvan Kolossvary, Mark A. Moraes, Federico D. Sacerdoti, John K. Salmon, Yibing Shan, David E. Shaw, Scalable algorithms for molecular dynamics simulations on commodity clusters, in: *Proceedings of the ACM/IEEE Conference on Supercomputing (SC06)*, Tampa, Florida, 2006, November, pp. 11–17.
- [59] Schrödinger Release 2019-1; Desmond Molecular Dynamics System, D.E. Shaw Research, New York, NY, USA, 2019. Maestro-Desmond Interoperability Tools, Schrödinger: New York, NY, USA, 2019.
- [60] R.A. Friesner, R.B. Murphy, M.P. Repasky, L.L. Frye, J.R. Greenwood, T.A. Halgren, P.C. Sanschagrin, D.T. Mainz, Extra precision glide: docking and scoring incorporating a model of hydrophobic enclosure for protein–ligand complexes, *J. Med. Chem.* 49 (2006) 6177–6196.
- [61] R.A. Friesner, J.L. Banks, R.B. Murphy, T.A. Halgren, J.J. Klicic, D.T. Mainz, M. P. Repasky, E.H. Knoll, M. Shelley, J.K. Perry, Glide: a new approach for rapid, accurate docking and scoring. 1. Method and assessment of docking accuracy, *J. Med. Chem.* 47 (2004) 1739–1749.
- [62] T.A. Halgren, R.B. Murphy, R.A. Friesner, H.S. Beard, L.L. Frye, W.T. Pollard, J. L. Banks, Glide: a new approach for rapid, accurate docking and scoring. 2. Enrichment factors in database screening, *J. Med. Chem.* 47 (2004) 1750–1759.
- [63] Schrödinger Release 2019-1: Glide, Schrödinger, LLC, New York, NY, 2019.
- [64] Y. Hai, D.W. Christianson, Histone deacetylase 6 structure and molecular basis of catalysis and inhibition, *Nat. Chem. Biol.* 12 (9) (2016) 741–747. #.
- [65] A.J. Jennings, J.R. Somoza, C. Mol, J.J. Buggy, A. Arvai, B.A. Katz, R.J. Skene, E. Chi, C. Luong, J.D. Ho, Structural snapshots of human HDAC8 provide insights into the class I histone deacetylases, *Structure* 12 (7) (2004) 1325–1334.
- [66] M. Holcomb, Y.T. Chang, D.S. Goodsell, S. Forli, Evaluation of AlphaFold2 structures as docking targets, *Protein Sci.* 32 (1) (2023).
- [67] V. Scardino, J.I. Di Filippo, C.N. Cavasotto, How good are AlphaFold models for docking-based virtual screening? *iScience* 26 (1) (2023).
- [68] T.J. Lane, Protein structure prediction has reached the single-structure frontier, *Nat. Methods* 20 (2) (2023) 170–173.
- [69] F. Ren, X. Ding, M. Zheng, M. Korzinkin, X. Cai, W. Zhu, A. Mantsyzov, A. Aliper, V. Aladinskiy, Z. Cao, S. Kong, X. Long, B.H. Man Liu, Y. Liu, V. Naumov, A. Shneyderman, I.V. Ozerov, J. Wang, F.W. Pun, D.A. Polykovskiy, C. Sun, M. Levitt, A. Aspuru-Guzik, A. Zhavoronkov, AlphaFold accelerates artificial intelligence powered drug discovery: efficient discovery of a novel CDK20 small molecule inhibitor, *Chem. Sci.* 14 (6) (2023) 1443–1452.
- [70] L. Lai, G.Y. Shin, H. Qiu, The role of cell cycle regulators in cell survival—dual functions of cyclin-dependent kinase 20 and p21cip1/waf1, *Int. J. Mol. Sci.* 21 (2020) 1–14.
- [71] F. He, X. Wang, Q. Wu, S. Liu, Y. Cao, X. Guo, S. Yin, N. Yin, B. Li, M. Fang, Identification of potential ATP-competitive cyclin-dependent kinase 1 inhibitors: de novo drug generation, molecular docking, and molecular dynamics simulation, *Comput. Biol. Med.* 155 (2023 Mar), 106645.
- [72] L. Whitehead, M.R. Dobler, B. Radetich, Y. Zhu, P.W. Atadja, T. Claiborne, J. E. Grob, A. McRiner, M.R. Pancost, A. Patnaik, W. Shao, M. Shultz, R. Tichkule, R. A. Tommasi, B. Vash, P. Wang, T. Stams, Human HDAC isoform selectivity achieved via exploitation of the acetate release channel with structurally unique small molecule inhibitors, *Bioorg. Med. Chem.* 19 (15) (2011 Aug) 4626–4634.
- [73] J. Liu, Y. Yu, J. Kelly, D. Sha, A.B. Alhassan, W. Yu, M.M. Maletic, J.L. Duffy, D. J. Klein, M.K. Holloway, S. Carroll, B.J. Howell, R.J.O. Barnard, S. Wolkenberg, J. A. Kozlowski, Discovery of highly selective and potent HDAC3 inhibitors based on a 2-substituted benzamide zinc binding group, *ACS Med. Chem. Lett.* 11 (12) (2020 Dec 10) 2476–2483.
- [74] E.F. Bülbül, J. Melesina, H.S. Ibrahim, M. Abdelsalam, A. Vecchio, D. Robaa, M. Zessin, M. Schutkowski, W. Sippl, Docking, binding free energy calculations and in vitro characterization of pyrazine linked 2-aminobenzamides as novel class I histone deacetylase (HDAC) inhibitors, *Molecules* 27 (8) (2022 Apr 14) 2526.
- [75] P. Aramsangtienchai, N.A. Spiegelman, B. He, S.P. Miller, L. Dai, Y. Zhao, H. Lin, HDAC8 catalyzes the hydrolysis of long chain fatty acyl lysine, *ACS Chem. Biol.* 11 (10) (2016) 2685–2692.